Spring 2017

Environmentally Friendly Synthesis of Transition Metalorganic Hybrid Nanocomposites

Aubrey N. Penn
aubrey.penn805@topper.wku.edu

Follow this and additional works at: https://digitalcommons.wku.edu/theses

Part of the Materials Chemistry Commons, Nanotechnology Fabrication Commons, and the Physical Chemistry Commons

ENVIRONMENTALLY FRIENDLY SYNTHESIS OF TRANSITION METAL-
ORGANIC HYBRID NANOCOMPOSITES

A Thesis
Presented to
The Faculty of the Department of Chemistry
Western Kentucky University
Bowling Green, Kentucky

In Partial Fulfillment
Of the Requirements for the Degree
Master of Science

By
Aubrey Penn

May 2017

ENVIRONMENTALLY FRIENDLY SYNTHESIS OF TRANSITION METAL-ORGANIC HYBRID NANOCOMPOSITES

Date Recommended 4/20/2017

_____
Dr. Hemali Rathnayake, Director of Thesis

_____
Dr. Kevin Williams

_____
Dr. Matthew Nee

_____   _____
Dean, Graduate School   Date   4/24/17

For their unending love and support, I dedicate this thesis to my parents.

ACKNOWLEDGEMENTS

There are a considerable number of people to thank for the completion of my graduate thesis. Without their hard work and support, this would not have been possible.

I would, first, like express my deepest gratitude to my research advisor, Dr. Hemali Rathnayake. She has devoted her time to me as a student, researcher, and person. I am appreciative for the many opportunities experienced because of Dr. Rathnayake's effort and commitment as an advisor. None of this would have been possible without her willingness to invest in me.

Second only to my advisor is Dr. John Andersland. I would like to thank him for teaching me the invaluable skill of electron microscopy, but also serving as an informal mentor in life. To my thesis committee, I am appreciative of Dr. Kevin Williams and Dr. Matthew Nee for their patience throughout my graduate process. Next, I would like to thank the Chemistry Department Head, Dr. Stuart Burris, for giving me the opportunity to conduct my research at Western Kentucky University.

To my research group, I am grateful for the shared research experience and friendships formed. I would like to especially thank Dr. Ananthakrishnan Soundaram Jeevarathinam, Danielle Chavis, and Hunter Sims for their commitment to my success.

Finally, I send my thanks to my dearest friends in the department, Haleh Jeddi, Sara Botero, and Jesús Berlanga. These three incredible chemists have brought laughter in considerably demanding times.

CONTENTS

LIST OF FIGURES

LIST OF TABLES

ENVIRONMENTALLY FRIENDLY SYNTHESIS OF TRANSITION METAL-ORGANIC HYBRID NANOCOMPOSITES

Aubrey N. Penn   May 2017   78 Pages

Directed by: Hemali Rathnayake, Kevin Williams, and Matthew Nee

Department of Chemistry   Western Kentucky University

Research on metal nanoparticles (MNPs) synthesis and their applications for optoelectronic devices has been a recent interest in the fields of nanoscience and nanotechnology Photovoltaics are one of such systems in which MNPs have shown to be quite useful, due to unique physical, optical, magnetic, and electronic properties, including the metal nanoparticles synthesized in this research.

Owing to the challenges with the most common physical and chemical methods of preparing MNPs, including the use of high temperatures, toxic reducing agents, and environmentally hazardous organic solvents, there is a critical need for a benign synthesis procedure for MNPs. In this work, a simple, versatile, and environmentally and economically responsible synthesis method for making iron, nickel, zinc, and bimetallic alloy nanoparticles (ANPs) has been developed and functionalization with organic capping agents were performed to form metal-organic hybrid nanocomposites with tunable properties. The size, shape, elemental composition, photophysical properties, and crystallinity of particles and their hybrids have been evaluated.

Monometallic nanostructures of iron, nickel, and zinc oxide were synthesized via aqueous-phase reduction of metal(II) chloride salts with sodium borohydride. Upon optimization of the standard method described here, reaction parameters like reaction time, reagent molar ratios, and capping-agent molar ratio were evaluated. Characterization

techniques such as transmission electron microscopy (TEM), scanning electron microscopy (SEM), energy-dispersive x-ray (EDS), IR, and UV-visible spectroscopies, selected area electron diffraction (SAED), and power x-ray diffraction (XRD) were performed as necessary. Well-defined, reproducible nickel and iron nanoparticles were produced with average diameters of 26 ± 4 nm and 50 ± 26 nm, respectively, arranged into chain-like structures. Much smaller (6-9 nm) zinc oxide particles that self-assembled into single-particle thick, hexagonal hierarchical microstructures were formed from a modified standard method. Similarly, iron-nickel ANPs with the average size of 20.9 ± 3.3 nm were also synthesized and successful grafting with the polymer capping agent, polyvinylpyrrolidone was confirmed.

Because of size, ordered self-assembly, and benign synthesis procedure, the nanoparticles described here are ideal candidates for photovoltaic and thermoelectric device applications. Moreover, these particles have shown to disperse well in various organic and inorganic media, and therefore have wide versatility in thin-film deposition methods.

CHAPTER 1

INTRODUCTION

1.1 Research Overview

Nanoscience is a quickly growing field of research referring to the study of materials and their characteristics of size ranging from 1 to 100 nm. Species of this scale can take on differing optical, mechanical, physical, catalytic, electrical, and magnetic behaviors than their macroscale counterparts,[1–4] and have therefore been widely researched for their applications in biomedicine, electronics, and materials engineering.[4,5] Among these applications, metal nanoparticles (MNPs), alloy nanoparticles (ANPs), and metal-organic hybrid (MOH) nanocomposites have become an increasingly popular research area. The unique optical and electrical properties of MNPs can be fine-tuned by manipulating their morphology. For example, spherical and cubic nanoparticles of the same material can have differing properties. The size of MNPs also affects optical and electrical properties, as is commonly observed in gold nanoparticles. A unique property of MNPs is the tendency of surface conduction band electrons to oscillate and absorb light when subjected to electromagnetic radiation. This phenomenon is called surface plasmon resonance (SPR), which possesses unique optical properties in MNPs.[6] Additionally, MNPs made from magnetic bulk materials have received attention due to their unique properties at the nanoscale. For example, orbital moments and spin moments are enhanced on the small surface of an individual particle.[4]

Many different transition metals including, but not limited to, copper (Cu),[7] palladium (Pd),[8] zinc (as ZnO),[9–15] titanium (as TiO_2)[16], silver (Ag),[17] nickel (Ni),[18,19] and gold (Au)[20] have been synthesized via various methods to form nanostructures of different morphologies including nanospheres,[7,10,16,18,19] rods,[11,12,15] plates,[20] flowers,[9,13,14] and

cubes.[17] Furthermore, bimetallic ANPs of many transition metals are widely studied including gold-silver (Au-Ag),[21–24] platinum-silver (Pt-Ag),[25] gold-cadmium (Au-Cd),[26] iron-nickel (Fe-Ni or FeNi$_3$),[2,27–37] silver-aluminum (Ag-Al),[38] and even trimetallic particles of gold-iron-platinum (Au-Fe-Pt)[39] and silver-copper-palladium.[40] Previous research has demonstrated alloy nanostructures with morphologies including cages,[25] dendrites,[33] chains,[28,30] wires,[26] and core-shells in addition to the shapes listed above.[2,4,21,22,24]

Au and Ag are the most commonly used metals in alloy nanoparticle research. These metals can be advantageous due to their catalytic activity, resistance to corrosion and oxidation,[21] SPR absorption in the visible range,[23,24] high electrical conductivity, and low resistivity.[41] The major disadvantage is the cost of these materials and their low resistance to ion migration,[42] which limits their use in large-scale applications. For this reason, there is a need to investigate alternatives that are lower in cost, but comparable in properties. Other transition metals such as nickel, iron, zinc, and their alloys have been investigated for the replacement of their noble metal counterparts in nanostructure systems.

Nickel nanostructures have been formed via varying physical, chemical, and biological processes in recent decades. Chemical methods such as chemical reduction,[18,19] microemulsion,[43] hydrothermal,[44] spontaneous[45] and thermal decomposition,[43] and microwave-assisted methods[46] have been studied. The factors controlling particle morphology in chemical methods include temperature and the molar ratios of reagents. Physical methods include thermal evaporation,[47] laser ablation, and ball-milling,[48] with temperature and reaction time as the primary controlling factors. Biological methods have

also been studied using plants and microorganisms for a highly efficient and "green" synthesis process, but can be lacking in morphology control.[49]

Iron nanoparticles are synthesized by similar methods and demonstrate behaviors analogous to nickel nanoparticles. Common methods include chemical reduction,[50] thermal decomposition,[51] vapor phase deposition,[52] and microemulsion.[53]

Zinc (as ZnO) is one of the most widely synthesized transition metals for its numerous scientific and commercial uses such as ceramics, electronics, catalysis, topical treatments, and cosmetics. The preparation methods to produce ZnO include, but are not limited to, thermal decomposition, solvothermal formation,[11] sol-gel,[54,55] solvent processing,[9] precipitation,[13,14] physical vapor deposition,[56] and biosynthesis.[10] Each of these methods has been extensively studied and have shown to produce ZnO nanoparticles with specific and consistent morphology.

ANPs, specifically of FeNi or FeNi$_3$, have made significant advancement in nanoscience research, with their synthesis being a prominent theme. Common wet synthesis methods include co-reduction,[2,31,32,34–36] hydrothermal formation,[33,37] microwave-assisted synthesis,[30] sol-gel,[57] and laser ablation in solution.[28] Novel electrochemical methods have also been reported,[5] and a number of research groups have tested biosynthesis methods for the production of these magnetic ANPs.[27]

Most of these preparation methods have several disadvantages when considering an environmentally and economically responsible synthesis process. The physical synthesis methods reported previously require expensive machinery and high levels of energy input, making the scaled-up reaction infeasible. Biological methods, while having the greatest potential for environmental benignity, still require in-depth research to fine-tune the

methodology. These methods tend to produce particles that are not consistent in morphology. It is widely accepted that chemical synthesis is the simplest, most versatile, and most economical method for both MNPs and ANPs. These wet synthesis procedures almost exclusively require heat, use toxic reducing agents, and are run in organic media. Therefore, there is an increasing demand for an environmentally conscious synthesis process.

There is much research focused on the incorporation of organic materials into nanoparticle structure to form nanocomposites with specific properties. Organic capping agents (CAs), or surfactants, are often used to control particle morphology, while also tailoring the properties of MNPs. CAs interact with NPs throughout particle formation to control growth and aggregation. These materials can also serve to functionalize the particle, often making them biocompatible or adjusting the optical and electrical properties. For example, polyvinylpyrrolidone (PVP) is an insulating polymer CA used to encapsulate toxic nanoparticles in a nontoxic shell for medicinal uses. Semiconducting CAs can also be used for electronic device applications to adjust electromagnetic absorption and tune the particles' band gap. CAs can also serve to protect MNPs from oxidation and corrosion in air or solution. Other common CAs include long chain hydrocarbons, polymers, chiral ligands, dendrimers, cationic surfactants, and polycarboxylic acids.[58]

1.2 Research Goals

The focus of my thesis is to develop of an economically and environmentally responsible, versatile synthesis method for preparing MOH nanostructures of various transition metals and their alloys with a variety of organic polymer CAs. These capped MNPs will be incorporated into application of electronic devices, particularly for organic

solar cells. Each material used and parameter followed is consciously considered in alignment with 7 of the 12 Principles of Green Chemistry outlined by the American Chemical Society, specifically;

    (1) Waste prevention,

    (2) Atom economy,

    (3) Less hazardous chemical syntheses,

    (4) Safer solvents and auxiliaries,

    (5) Design for energy efficiency,

    (6) Reduced derivatives,

    (7) Inherently safer chemistry for accident prevention.

A bottom-up synthesis approach, which involves the building up of structures atom-by-atom, was used to accomplish the following objectives:

Objective 1: Synthesize Ni, Zn, and Fe metal and $FeNi_3$ alloy nanoparticles via aqueous-phase reduction of their respective inorganic salts at room temperature.

Objective 2: Study particle morphology with respect to parameters such as reaction time, molar ratio of reagents, injection rate, and injection method.

Objective 3: Graft MNPs with polyvinylpyrrolidone.

CHAPTER 2

BACKGROUND

2.1 Overview

Nanoparticles have played a role in nature far before humans had the ability or knowledge to detect and study them. For example, gold and silver nanoparticles of various sizes are responsible for coloring of stained glass windows centuries.[2] With technological advances, our ability to observe and analyze increasingly minute substances has allowed for the manipulation of nanoscale materials for their optical, physical, electronic, and chemical properties. Unique from their large-scale counterparts, such properties are dependent upon the particles' morphology. Many recent advances in nanoscience focus on the synthesis of nanomaterials and their applications to a variety of biomedical, electronic, chemical, environmental, and industrial fields. The following is a compilation of some of the most significant recent advances in nanoparticle synthesis, focusing primarily on transition MNPs, their bimetallic alloys, and MOH nanocomposites.

2.2 Nanoparticle Synthesis Approaches

Synthesis approaches for nanomaterials fall into two categories: top-down and bottom-up synthesis. The top-down synthesis approach involves the breaking of a macroscale material down to its nanoscale components. Some of the more common methods for top-down synthesis are ball-milling,[48] sputtering,[48] and laser ablation.[59] While highly efficient at producing large quantities of nanomaterials, top-down synthesis approaches usually lead to particles with less controllable morphologies and can lack reproducibility. Conversely, the bottom-up synthesis approach involves the building of clusters by atom, ion, or molecule. Wet chemical processes are most commonly employed for bottom-up synthesis due to their low cost, safety, and high degree of control over

reaction parameters.[59] For these reasons, bottom-up wet chemical syntheses are often preferable to top-down approaches.

2.3 Metal and Alloy Nanoparticle Synthesis Methods

Increasingly, the synthesis methods of MNPs are being used in more applications and has developed into large-scale production of MNP. If the principles of green chemistry principles are not applied, MNP production can be highly harmful to the environment. However, current green methods of MNP synthesis have reduced efficacy.[1] Many of the previously reported MNP and ANP synthesis methods do not take environmental impact into account. Synthesis methods can be categorized as physical, biological, or chemical synthesis methods, and the most common of each of these categories have been outlined in the following sections.

2.3.1 Physical Methods for Metal and Alloy Nanoparticle Synthesis

Physical methods for MNP and ANP synthesis have proven to be quite effective for large-scale production, and have their own set of advantages. Many physical methods do not require other toxic chemicals or solvents, which comprise at least 80% of the materials used in chemical manufacture.[1] Physical methods are categorized under the top-down approach, and therefore are fast and generally easy to perform. However, physical methods can be expensive because they often require expensive equipment, elevated temperatures, and vacuum conditions. The selected methods described below are the most common physical synthesis methods for metals of interest—nickel, iron, ZnO, and FeNi$_3$ alloy

2.3.1.1 Vapor Phase

Vapor phases syntheses include methods such as pulsed laser ablation, sputtering, thermal evaporation.[47,52,56] In these syntheses methods, a bulk material is converted to the gas-phase, leading to supersaturated vapor, and particles are then formed as the vapor condenses onto a substrate. The material used, the temperature of the vapor, and the atmosphere are the primary factors affecting particle shape, size, and aggregation behavior.[47]

Pulsed laser ablation uses a high-energy laser directed at the material to form a plume that condenses over only a small area. This method is not appropriate if large quantities of particles are needed, but pulsed laser ablation can be used to evaporate materials that do not readily do so by other methods. Pulsed laser ablation can be used for metals, but is also applicable with many other materials. Additionally, sputtering is a method used almost entirely for metal targets. Particles are formed by sputtering at low pressures with a beam of inert gas ions.[47]

Thermal evaporation is another vapor phase method used for MNPs, with variables including pressure, evaporation time, and inert gas flow rate if not under vacuum. Pan, et al., demonstrated the formation of several metal oxide nanostructures via thermal evaporation. ZnO nanobelts of lengths up to several millimeters and well-defined crystalline structure were formed using thermal evaporation.[56] Disadvantages to vapor syntheses are the high energy input required for high temperatures and the inability to control nanoparticle aggregation.[47]

2.3.1.2 Mechanochemical Synthesis

Commonly known as ball milling. Mechanochemical synthesis methods are top-down processes, often involving the breaking down of a bulk material to its micro or nanoscale components. Mechanochemical methods also encompass substitution or degradation reactions in the solid phase. There are several advantages to considering MNP synthesis with this method. Solvents are not usually used in ball-milling techniques, so chemical cost, waste, and reaction procedures are lessened. These processes are run at room temperature and are easily scaled up, so when considering commercialization, ball-milling can be an attractive option. MNPs and metal oxides are commonly produced with mechanochemical techniques.[48] Huber explains that iron nanoparticles and composites can be formed by reactive ball-milling of iron oxides in the presence of alumina. Lack of morphology control is the major disadvantage of this process.[52]

2.3.2 Biological Methods for Metal and Alloy Nanoparticle Synthesis

Biological synthesis methods are considered to be the most environmentally benign pathways for MNP formation. These syntheses include the use of microorganisms such as bacteria, fungi, viruses, and plants as the reaction vessel for MNP synthesis due to the intracellular chemical conditions. Other biological materials such as proteins, peptides, or DNA are also being used as reducing agents or templates for MNP growth. To date, gold and silver nanoparticles are the most commonly used metals for these syntheses, but they have been applied with other materials.[1,27,49] Sarkar, et al., reports the extracellular formation of solution-stable ZnO nanoparticles using the fungus, *A. alternata*.[10] Iron oxide, in the form of magnetite, was synthesized with *F. oxysporum* and *Verticillium* by hydrolyzing iron with the secretions from these fungi.[60] FePt magnetic ANPs were

produced using peptides as growth templates in work described by Reiss, et al.[27] Finally, Iravani reports on the synthesis of titanium-nickel ANPs, iron oxide, and ZnO nanoparticles using a variety of plants and plant extracts including *Aloe vera*, alfalfa, and rose geranium plants.[49] These pathways have shown to be eco-friendly and produce highly stable particles due to the incorporation of proteins, etc. into the structure of the particles. The major disadvantage of these syntheses is the lack of morphology control. Particles produced by biological methods are consistently polydispersed.[1,10,27,49,60]

2.3.3 Chemical Methods for Metal and Alloy Nanoparticle Synthesis

Wet chemical synthesis methods are the most commonly used synthesis routes for the formation of MNP and ANP. Solution-based nanoparticle synthesis has been shown to be the most effective method due to control over reaction parameters that affect particle nucleation and growth. The chemical routes for these types of syntheses are quite diverse, but can generally fall under several main categories, described in the following sections.

2.3.3.1 Thermal Decomposition

Thermal decomposition synthesis methods are commonly used for a variety of MNPs. This method involves the decomposition of a metal compound or complex with the addition of significant heat. Organometallic precursors are commonly used in these synthesis methods because of their ease of reduction at such high temperatures and the enhanced control over particle surface morphology and size.[45] Although the exact mechanism for MNP formation via thermal decomposition is not well known. Decomposition mechanisms are often extraordinarily complicated, depending on the metal precursor used.[52] It is understood that particle nucleation and growth are separate processes. Park, et al., hypothesized that nucleation occurs at the low-temperature stage of

the reaction, and growth occurs at higher temperatures. Therefore, particle size can be controlled by decomposition temperature. Work from the Park group also explored the effect of molar ratios of iron precursor to the capping agent of choice, oleic acid, and showed that particle size was able to control with the synthesis process and the deviation of the particle size was less than 5%.[51] In one study, alkylamines were used to produce nickel nanoparticles by thermal decomposition. Alklyamines serve as both the solvent and the reducing agent for this synthesis approach.[43] The simplicity, lack of complex by-products, and highly controlled morphologies of MNPs produced from thermal decomposition make it an advantageous over other synthesis approaches. Though this method gives highly consistent results, the use of high levels of heat is a limiting factor for large-scale production.

2.3.3.2 Hydrothermal Methods

Hydrothermal processes refer to a wide set of processes, but with two essential parameters in common: an aqueous medium and elevated temperature. An autoclave is commonly used for this synthesis method to ensure consistent heating across the entire solution and high pressures, minimizing factors, which could affect particle morphology. This synthesis technique is advantageous as well since it does not require harsh, toxic chemicals, and rather depends on heat and long treatment times. Hydrothermal routes have shown to produce particles with well-defined morphologies. A study on nickel nanoparticle synthesis by this route produced nanobelts with no metal oxide contamination and well-defined crystal structure by 24 hour hydrothermal treatment of nickel tartrate.[44] Hydrothermal methods make up approximately a quarter of the chemical synthesis methods used to form iron nanoparticles. In a specific study it was found that iron precursor

concentration is directly proportional to particle size, but residence time in the autoclave has the greater impact.[61] Wang and coworkers found that with $FeNi_3$ ANPs, the surfactant used directly affected the particle shape in their hydrothermal approach. For example, spherical particles were produced with polyethylene glycol, and sea-urchin-like particles were produced with cetyltrimethylammonium bromide (CTAB).[62] Hydrothermal methods have been explored without surfactants as well. For example, Zhou and Wei described a surfactant-free hydrothermal process forming $FeNi_3$ dendrites where morphologies were directly affected by solution temperature, reaction time, and reagent concentrations.[33] Flower-like particles and hollow spheres where also reported.[37,63] Jang, et al., showed that the pH of the solution in hydrothermal processes dramatically affected the morphology of ZnO structures formed.[64] The major disadvantages of hydrothermal synthesis are the long reaction time and high temperatures required, limiting their applicability in the large-scale.

2.3.3.3 Sol-gel Method

The sol-gel method is one of the most widely used forms of nanoparticle formation for a wide variety of organic and inorganic nanoparticles. In the sol-gel process, a solution (sol) converts to a gel-like system with a solid and liquid phase. The system is governed by colloid chemistry in which the solid-phase particles interact with each other through van der Waals or electrostatic forces. Metal oxides are the most commonly formed by this process.[65] For example, the Chung group designed a sol-gel method in which a zinc oxalate gel was formed in a solution of ethanol, oxalic acid, and zinc acetate. The zinc oxalate served as a precursor to ZnO nanoparticles formation. High-temperature calcination was performed to decompose zinc oxalate to ZnO, thus forming nanoparticles. Reaction parameters such as reagent concentration and calcination temperature all had direct impact

12

on particle size.[54] Work by Omri, et al., also used an ethanol-based sol-gel method followed by thermal treatment to form ZnO particles with well-defined morphology.[55] FeNi$_3$ ANPs were produced by a unique, but inefficient method, which requires approximately 30 g of metal precursor to produce 1 g of alloy product. With the requirement of higher precursor load and extremely high temperatures, sol-gel synthesis makes inefficient and economically challengeable for large scale production.[57]

2.3.3.4 Colloidal Microemulsion

Microemulsions are formed by nano-sized water droplets in oil stabilized by surfactants at the water-oil interface. Colloidal microemulsion synthesis employs unique microenvironments that occur at phase interfaces to form metal nanoparticles. A plethora of metal-based materials have been formed using this technique, but a particular study by the Chen group showed the formation of nickel nanoparticles via hydrazine reduction at a water/CTAB interface. Highly monodispersed spherical nanoparticles were produced with the primary morphology controlling factor being CTAB concentration.[66] In a similar method, iron-iron oxide core-shell nanoparticles were prepared in a water/CTAB/oil microemulsion via NaBH$_4$ reduction. In this method a higher water-to-oil ratio produced spherical particles of smaller size.[53]

2.3.3.5 Microwave-assisted Method

The use of microwave irradiation in synthesis processes has become increasingly popular due to repeatedly demonstrating its ability to form nanostructures quickly and economically. Microwave irradiation, applied to MNP synthesis methods, has shown to form "hot spots" due to the absorbing characteristics of MNPs. These hot spots drive the fusion of monomers into crystalline structures and crystal growth. A particular example is

that of Jia, et al., who performed microwave-assisted hydrothermal synthesis of $FeNi_3$ ANPs arranged into highly ordered chains. The synthesis process was performed in two 5-min steps, which is considerably faster than other comparable methods.[30] Nickel nanoparticles have also been synthesized via microwave-assisted methods such as the polyol reduction of nickel salt in the presence of various capping agents reported by Li, et al. Although fairly polydispersed, nickel nanoparticles with minimal aggregation were produced with this quick method.[46]

2.3.3.6 Chemical Reduction and Co-reduction

The chemical reduction of metal salts is the simplest, most common method for MNP synthesis, and is the method used in the research presented in this thesis. Chemical reduction involves the conversion of metals from high oxidation states, such as Ni^{2+} and Fe^{2+}, to lower oxidation states to form nanostructures. Chemical reduction is achieved by several agents including sodium borohydride,[50,67] hydrazine,[68] polyols,[18,19,69,70] and polysaccharides.[1] These methods offer flexibility of synthesis with a variety of reaction parameters that can be manipulated to form the most ideal structures for the intended application. The major disadvantages to chemical reduction methods are undesired metal oxide formation and particle aggregation, which can both be minimized with the use of organic capping agents, or surfactants.[58] The selected literature, described below, evaluates one or more of the specific parameters that control MNP morphology such as precursor molar ratios, capping agents, reaction time, and temperature and are summarized in Table 1.

Table 1. Summary of MNP and ANP Chemical Reduction Methods as Reported by Literature.

Metal	Solvent	Reducing Agent	Capping Agent	Morphology	Reference
Ni	Triethylene Summary of MNP and ANP chemical reduction methods as reported by literature Glycol (TEG)	TEG	PVP	Minimally aggregated spherical particles, ~300 nm	16
Ni	Ethylene glycol (EG)	N_2H_2	(EG)	Polydispersed spherical particles, 175±36 nm	15
Ni	Polyethylene glycol (PEG)	PEG	Oleic acid	Aggregated particles, 15 nm	70
Ni	EG	N_2H_2	EG	Monodispersed spherical particles, ~6 nm	69
Ni	water	N_2H_2	PVP	Polydispersed particles, 20-50 nm	67
Fe	Ethanol/water	$NaBH_4$	PEG	Core-shell particles, 10-20 nm	66
FeNi	water	N_2H_2	Pyridinium derivatives	Aggregated spherical particles, 80-140 nm	29
FeNi	water	N_2H_2	none	Nanoplatelets, 23-92 x 10 nm	34
FeNi	water	N_2H_2	none	Spheres to nanoplatelets	30

The polyol method is quite popular for MNP synthesis because the reducing agent can double as the solvent or capping agent. Moreover, these syntheses can be run in inert atmosphere.[18,19] The method performed by Roselina, et al., is a simple, quick polyol synthesis approach involving hydrazine and heat. In this procedure, nickel nanoparticles increased in size and polydispersity widened with increased reaction time.[18] Hexagonal

close-packed (*hcp*) nickel nanoparticles were synthesized by Guo, et al., in a more complex procedure. Pure nickel crystallizes into two forms: face-centered cubic (*fcc*) and *hcp* phases, but *hcp* is considered metastable. Therefore, the formation of such a crystal structure is a significant achievement. The hexagonal close packed nanoparticles were formed with triethylene glycol as the solvent and reducing agent in the presence of PVP, which was concluded to be responsible for the *hcp* crystal structure.[19] Rao and coworkers also used polyols method to make well-ordered hcp nickel nanoparticles, which were formed in low nickel precursor concentrations and high temperatures. Although, there are several advantages to the polyol method, such as quick reaction times and atom economy, the use of organic solvents and heat leave room for improvement when considering the green chemistry principles.

Hydrazine is a common reducing agent used in many nanoparticle syntheses. A major disadvantage to this chemical, though, is its high toxicity. In a study performed by Chou, et al., NaOH was used as a catalyst along with polyols and hydrazine to evaluate parameters such as NaOH concentration and temperature on nickel nanoparticle morphology. It was found that NaOH concentration had a much more significant influence than temperature.[70] It was determined from another nickel nanoparticle synthesis method that hydrazine reduction occurs entirely within five minutes, and these particles formed best in solution at a pH value of 12.[68]

Reduction by sodium borohydride is a safer alternative to hydrazine reduction, and can be performed in the aqueous phase. After reduction, sodium borohydride decomposes to less toxic components, producing hydrogen gas as a by-product. Using sodium borohydride reduction, iron-organic core-shell nanostructures were prepared in an

ethanol/water solution, pressurized through a Y-tube under inert nitrogen atmosphere. In this case, the flow rate of the reducing agent determined the particle morphology.[67] It is worth noting that chemical reduction methods are not common for iron nanoparticles synthesis as for other metals. This is due to the fact that most iron nanoparticles are in the form of iron oxides, and are therefore more commonly synthesized by physical or thermal methods.

Polysaccharide reduction is considered to be one of the most environmentally benign chemical reduction methods for MNP synthesis due to their non-toxicity, and water-solubility. The hydroxyl groups on polysaccharides such as β-D-glucose, negatively charged heparin, and amylose (starch) make the reduction of metals and semiconducting precursors possible. However, the strong inter- and intramolecular hydrogen bonding in these sugar structures leads to aggregation. Additionally, starch-MNP binding strength is weak compared to other metal nanoparticles, so the removal of capped sugars does not present an issue.[1]

Co-reduction refers to the reduction of two metal precursors to form ANPs. Like its monometallic counterpart, co-reduction is performed in a variety of media and with several different reducing agents. Capping agents are also commonly utilized to stabilize ANPs or to fine-tune their chemical and physical properties. Alloys can arrange themselves into a few different crystal structures, shown in Figure 1. Metallic monomers can arrange themselves into core-shell, subclusters, and mixed alloys. Subclusters are less common, and mixed alloy particles, whether ordered or unordered, are quite common in ANP synthesis. In bimetallic reduction, the material with the highest reduction potential is typically reduced first forming a core on which the lower reduction potential metal reduces

and forms a shell. Successive, or sequential, reduction can be used to form nanostructures with multilayered morphology. This is achieved by the reduction of a particular material followed by successive reductions with the original particles present, acting as seed particles.[2]
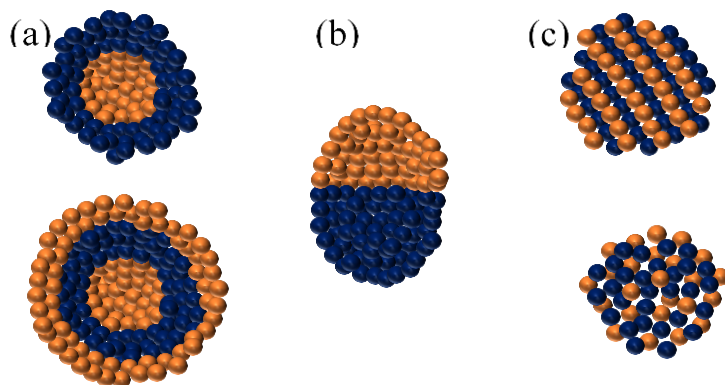
Figure 1. Possible structures of ANPS: (a) core-shell (b) subclusters (c) ordered and unordered mixed alloys.

Here, we will focus on several chemical reduction methods (similar to those for monometallic systems) used for the synthesis of iron-nickel ANPs. Hydrazine and sodium borohydride are the most common reducing agents, and capping agents are sometimes used to enhance particle stability, stabilize surface energy, and control aggregation and growth. Three separate $FeNi_3$ ANP synthesis procedures are run in the aqueous phase with a hydrazine reducing agent, one pyridinium derivative capping agents.[31] In work performed by the Wang[36] and Hongxia[32] groups, nanoplatelets were formed. Wang et.al. explains the control of platelets size being due to the concentration of metal precursors affecting particle nucleation and aggregation. Meanwhile, the shift in nanostructure shape from spheres to platelets in the report by Hongxia, suggests that the method of solution agitation controls morphology. Three separate experiments were performed in which no stirring, stirring, and

ultrasonic irradiation agitation methods were evaluated. It was found that spherical particles were formed in the unstirred solution, a combination of spheres and platelets were formed in the stirred solution, and exclusively platelets were formed in ultrasonic irradiation sample.[32]

These synthesis methods, while shown to be effective, could be improved greatly by considering green synthesis methods. Water is the most ideal solvent for benign syntheses, sodium borohydride is advantageous due to its mild nature and tendency to decompose in water, and the lack of heat input to the system is highly advantageous when considering the scaled-up synthesis and economic factors.

2.4 Metal Nanoparticle Formation Mechanism

Although significant research has been performed regarding the synthesis and applications of MNPs, there is little understood about how reaction parameters control particle growth. There are not well-defined mechanisms describing how synthesis conditions directly affect the mechanism for MNP formation, only hypotheses or computationally supported ideas. Nucleation approaches are justified thermodynamically, kinetically, or stoichiometrically. For wet chemical reduction methods, several models include nucleation, LaMer's theory, diffusion limited growth, and Ostwald ripening.[71]

2.4.1 Nucleation

Classical nucleation theory (CNT) is a model based entirely on thermodynamics—minimizing the Gibb's free energy of the system—but does not describe particle growth. CNT can be categorized by heterogeneous and homogeneous nucleation. As a preferred mechanism, heterogeneous nucleation occurs at the solid-liquid interface of a solution. Solid contaminants or seed particles are required for this type of nucleation, as the

nucleation begins on the solid surface. The surface of the solid is of a lower effective surface energy, thus reducing the activation energy of the nucleation process. In contrast, homogeneous nucleation occurs randomly and spontaneously, and requires a supercritical state of the solution. It is hypothesized that these two mechanisms occur simultaneously in solution, with heterogeneous nucleation favored.[71]

2.4.2 LaMer's Nucleation Theory

The LaMer model, also referred to as burst nucleation, is the most widely accepted model for MNP nucleation. This model separates the idea of nucleation and growth, beginning with slow homogeneous formation of monomers. The minimum monomer concentration is reached so that the activation energy is overcome, and rapid nucleation can occur. This is known as the burst nucleation, after which the monomer supersaturation level decreases below the minimum concentration value, thus ending particle nucleation, and beginning particle growth.[71]

2.4.3 Diffusion Limited Growth

The diffusion limited growth model, described by Howard Reiss, is a simple model explaining that particle size is dependent entirely on monomer flux through solution. He described that smaller particles move and grow more quickly than larger ones in solution, and therefore consistent particle sizes could be derived from solutions where varying nucleation rates were occurring. Reiss' model is too simplified though, not taking into account particle aggregation or dissolution. [71]

2.4.4 Ostwald Ripening

The mechanism of Ostwald ripening is a purely thermodynamically driven system. The idea here is that larger particles are more stable, and are therefore thermodynamically

preferred to higher energy small particles. The atoms at the surface of MNPs are the least stable, so in smaller particles, these more active particles are released into the solution. Once saturation is met, the free particles begin to deposit onto the more stable large particles, therefore small particles get smaller and large particles get larger. This mechanism is considered to be "size focusing" due to the rapid disappearance of small particles and the slow rate at which large particles grow—as they get larger, their growth rate decreases.[72]

2.4.5 Growth Mechanism with NaBH$_4$ Reducing Agent

The reduction of metal salts with NaBH$_4$ occurs faster than particle nucleation and growth (milliseconds or less to a several seconds), therefore a system is considered where many metal monomers are present in solution before any growth occurs. This system is dominated by coalescence (particles merging together), and is followed by solution aggregation, which is a behavior of unstable colloids, shown in Figure 2. Aggregation is most commonly combatted with the inclusion of a steric stabilizing agent, such as PVP, but in this study, PVP had no effect on colloidal stability. From this, it is concluded that particle growth and size are a result of colloidal stability. Because reduction and nucleation are separated in this model, it is suggested that the most controlled particle growth would be achieved if reduction occurred atom-by atom. Additionally, larger particles are less likely to aggregate than smaller particles.[71]
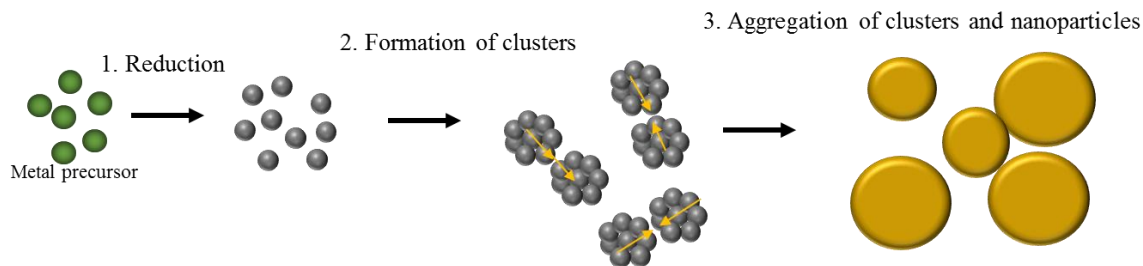
Figure 2. Schematic representation of nanoparticle growth after metal precursor reduction.

2.5 Applications of Metal, Alloy, and Metal-Organic Hybrid Nanostructures

Metals, alloys, and MOH composites are an increasingly popular area of nanoscience research due to their applicability across many fields of science. Properties of both metal and capping agent independently, and the properties developed upon combination can be advantageous in biomedicine, catalysis, and electronic devices.

2.5.1 Biomedicine

Metal nanoparticles capped with biocompatible organic molecules have shown significant application in the biomedical field in a variety of forms. Balakrishnan, et al., reports the use of PEG-coated iron nanoparticles as a valid form of hyperthermia treatment.[67] Drug delivery is another application for biologically inert-capped MNPs. [19] Ferromagnetic nanoparticles are being widely studied for their application in diagnostics, particularly in MRI diagnosis by acting as cellular labels or DNA/protein markers.[2]

2.5.2 Catalysis

The role of metal nanoparticles for various forms of catalysis have been widely studied for decades. Semiconducting nanostructures, such as ZnO, have applications in photocatalysis, such as photodegradation of organic materials to clean up waterways.[1]

Additionally single metal and alloys nanostructures have shown to be effective catalysts for petrochemical reactions[2] and as additives to fuel cells.[73]

2.5.3 Electronic Devices

With ever-growing global energy demands, there is a great need to replace fossil fuel-driven systems with more environmentally friendly energy harvesting technologies. This need has influenced researchers in many fields to focus their work on alternative energy systems, focused on the development and improvement of photovoltaic (PV) devices, also known as solar cells. The current commercially available silicon-based PVs, while demonstrating the highest efficiencies (20-25%)[74,75], are limited in widespread applicability due to expense of materials and production[76], kilowatt hour (kWh) cost,[77] and the large, rigid structure of panels. These negative factors of the current technology have initiated a vast field of research focused on generating novel PV technologies as simply, cheaply, and efficiently as possible through varying materials, architectures, and processes.

The application of both organic and inorganic materials, like those previously discussed, is advantageous to PV devices for a variety of reasons. While sometimes requiring expensive processing and being generally more toxic,[78] many inorganics can offer good electrical conductivity, tunable absorption, and environmental stability. Organic materials are also propitious, though, due to low cost, solution phase processing, flexibility, and high throughput.[75] In combination, organic-inorganic hybrid (OIH) composites can overcome several disadvantages of each independent material, increase device efficiency, and broaden PV functionalization and applicability.[79]

CHAPTER 3

MATERIALS AND METHODS

3.1 Materials

Iron(II) chloride tetrahydrate, zinc(II) chloride, sodium borohydride, ammonium hydroxide (28-30%), polyvinylpyrrolidone (PVP, M_W 40,000), and 200 proof anhydrous ethanol were all purchased from Sigma-Aldrich, and were used as received. Nickel(II)chloride hexahydrate was purchased from Fisher Scientific. Deionized water was brought to a boil and saturated by bubbling with argon before using in the experiments.

3.2 Characterization

A JEOL JEM-1400 Plus transmission electron microscope (TEM), and a JEOL 6510LV scanning electron microscope (SEM) equipped with IXRF i500 X-ray analysis systems were used to determine nanostructure morphology along with elemental composition analysis using energy dispersive X-ray spectroscopy (EDS). All TEM images were taken at an acceleration voltage of 80 kV, and all SEM images and EDS spectra were taken 20 kV. SEM analysis was performed at high vacuum mode with secondary electron imaging (SEI). A Perkin-Elmer Spectrum One FT-IR spectrometer was used to obtain FT-IR spectra. A Shimadzu UV-2600 UV-visible spectrometer was used for the characterization of photophysical properties in ethanol solution. The crystallinity of products was analyzed from X-ray diffraction (XRD), on an Oxford Gemini diffractometer, and selected area electron diffraction (SAED) using TEM.

3.3 Nickel Nanoparticle Synthesis

The reaction conditions described here were optimized by performing a series of reactions varying the $NaBH_4$ injection method and reaction time. Early reactions included the injection $NaBH_4$ solution into $NiCl_2$ solution by a burette, and the injection of $NiCl_2$

solution to NaBH$_4$ solution via siphoning. Additionally, several experiments were performed to evaluate the effect of Cu seeding on particle formation. Undesirable metal oxide formation was prevalent and reproducibility was not achieved. For this reason, siphoning had to be stopped, and the rest of the experiments were performed by needle injection through a septum with the solution flushed with argon. This series of experiments referred as the "standard method" throughout this thesis.

NiCl$_2$•6H$_2$O (0.3372 g, 1.419 mmol) was added to a 100-mL round bottom flask with a magnetic stir bar, and was dissolved in 30 mL of deionized water, mixing vigorously. The flask was flushed with argon. NaBH$_4$ (0.1980 g, 5.200 mmol) was dissolved in 5 mL of deionized water, and added to the reaction flask consistently over a 45-min period maintaining the flow rate at 0.11 mL/min. During this time, the solution turned from clear to bright green to a clear suspension of black solid, coagulating into chunks over time. After the 45-min injection period, the reaction was left to mix, under constant argon flow, for 1 h. The product formation was monitored by TEM by taking a small aliquot of solution from the reaction mixture after 1h of reaction time. The solid was isolated via centrifugation for 30 min. The black solid was washed several times with deionized water followed by ethanol to remove unreacted precursor and other by-products, and dried under vacuum for several hours. From this reaction, 0.0973 g of Ni nanoparticles were yielded

3.4 Iron Nanoparticle Synthesis

FeCl$_2$•4H$_2$O (0.5169 g, 2.600 mmol) was used for iron nanoparticle synthesis under the same conditions as the optimized nickel reactions. Solution color and precipitating tendencies were also similar to nickel, and same purification method was followed. Due to the particles' tendency to oxidize, the product was stored under vacuum

or nitrogen whenever possible. Particle formation was monitored by preparing samples for TEM at reaction times of 0, 15 min, 30 min, 1 h, and the dried solid re-dispersed in ethanol. From this experiment, 0.1152 g of Fe nanoparticles were yielded.

3.5 Zinc Oxide Nanoparticle Synthesis

Early reactions were performed in a similar method to early nickel-based reactions. Upon the abandonment of the siphoning method and the adoption of argon-flushed reactions, reaction conditions such as reaction time, and $NaBH_4$ molar ratios were adjusted for optimization.

Maintaining the same experimental procedure as for Fe and Ni particle formation, ZnO nanostructures were prepared by bringing the pH of the reaction mixture to ≥ 10 with NH_4OH prior to the addition of $NaBH_4$ solution. $ZnCl_2$ (0.3544 g, 2.600 mmol) was used at a 1:1 molar ratio with $NaBH_4$ (0.0984 g, 2.600 mmol). In this case, the solution was slightly cloudy and white, but with the addition of $NaBH_4$ it became a suspension of white solid, without the tendency to coagulate. From this experiment, 0.4251 g of Zn product was yielded. UV-vis spectroscopy did not demonstrate absorption in this region. FT-IR (cm^{-1}): 3430 (O-H), 735 (Zn-O).

3.6 Capped and Uncapped Iron-Nickel Mixed Alloy Nanoparticle Synthesis

In initial attempts, $FeNi_3$ nanoparticles were prepared by following the literature procedure published by Zhou, et al. This method was modified to more closely fall in line with green synthesis standards and minimize metal oxide formation. In a typical procedure, $NiCl_2 \cdot 4H_2O$ (0.5000 mg, 2.100 mmol), $FeCl_2 \cdot 4H_2O$ (0.1392 g, 0.7000 mmol), and 14 mL water were added to a 100 mL round bottom flask equipped with a magnetic stir bar, and was set to mix at room temperature under argon atmosphere. After mixing for

approximately 10 min, chilled 28% NH_4OH was added to the reaction solution drop-wise until a pH ≥ 10 was reached and the solution color was changed from clear to light green, to a suspension of a blue-green precipitate. In a reaction with capping agent, PVP (0.1237 mg, 20 wt. %) in 2 mL water was added to the reaction flask. This step is excluded in uncapped reactions. Next, $NaBH_4$ (0.4000 mg, 11.20 mmol) in 3 mL water was added slowly, avoiding overflow since there was significant effervescence. In reactions with PVP present, the effervescence was greater. The precipitate turned black with $NaBH_4$ addition. Argon flow was continued until the solution stopped fizzing. The solution was left to mix for 12 h, and the black solid was isolated via centrifugation, washed twice with ethanol, and dried under vacuum for several hours. Particle formation was monitored by preparing samples for TEM at reaction time of 12 h and dried solid after re-dispersed in ethanol.

In subsequent experiments, the weight percentage of PVP added was adjusted to observe capping agent concentration's effect on particle morphology. Separate trials had PVP concentrations of 5, 10, 30, 40 and 50 wt. %.

A trial was performed with the aforementioned metal salt molar ratios reacted with the standard method presented for nickel and iron monometallic nanoparticles. The only modified parameter was a $NaBH_4$ injection rate of 0.25 mL/min over 20 min. Solution color and precipitating tendencies were also similar to nickel, and purification methods followed were maintained.

3.7 Iron-Nickel Core-Shell Alloy Nanoparticle Synthesis

The Zhou method was modified further in an effort to produce more ordered, iron-nickel core-shell nanoparticles instead of the aforementioned alloy particles. $FeCl_2 \cdot 4H_2O$ (0.1392 g, 0.7000 mmol) was added to a 100-mL round bottom flask with a magnetic stir

bar, 7 mL of water was added, and the solution was set to mix at room temperature while the flask was flushed with argon. Chilled 28% NH_4OH was added dropwise until $pH \geq 10$ forming a blue-green precipitate. $NaBH_4$ (0.2112 g, 5.600 mmol) in 1.5 mL water was added slowly to the reaction flask, forming effervescence and causing the precipitate to turn black. Argon flow continued until effervescence ceased, and the solution was left to mix for 12 h at which time a small amount of product was removed for analysis. While still mixing and reintroducing argon flow, $NiCl_2 \bullet 6H_2O$ (0.500 g, 2.100 mmol), in 7 mL water, was added directly to the reaction flask. Another aliquot of $NaBH_4$ of the same concentration was added slowly to avoid excessive effervescence. Again, argon flow remained until effervescence ceased, and the reaction was left to mix for 12 h more, at which time the well-dispersed black solid was isolated via centrifugation. Particle formation was monitored by preparing samples for TEM of the intermediate Fe product and the final reaction solution and re-dispersed product in ethanol.

3.8 Sample Preparation for Electron Microscopy Analysis

Before the sample was deposited, 200-mesh carbon coated copper grids were plasma cleaned in a Torr International thermal evaporator at a power of 20 W, at a pressure of 5×10^{-2} torr of nitrogen gas, for 15 s. TEM samples were prepared by placing one drop of the given sample solution onto the plasma cleaned grids and dried in air. SEM samples intended for EDS analysis were prepared by dusting dried, purified sample on conducting carbon tape. Both grids and carbon tape were purchased from Electron Microscopy Sciences (tape product number: 77816).

CHAPTER 4

RESULTS AND DISCUSSION

4.1 Development of an Aqueous-Phase Synthesis Method to Make Nickel Nanostructures and their Characterization

4.1.1 Overview

Magnetic nickel nanoparticles have been shown to have many applications in biomedicine, sensors, catalysis, and electronic devices.[19,69,80] The unique properties of nanoparticles are a result of their small size, and are controlled by their morphology. Here, we describe the development of a simple, versatile, room temperature, aqueous-phase process to produce elemental nickel nanoparticles with controlled morphology and minimal aggregation. The reaction was carried out under inert gas atmosphere via the chemical reduction method in the presence of a mild reducing agent, sodium borohydride and without capping agents. Initial attempts were performed in ambient conditions, but produced amorphous structures with a lack of reproducibility. Varying conditions such as solution injection method, reaction time, reaction atmosphere, and the introduction of seed particles were tested. A more highly controlled reaction method was necessary to form the desired particles. This optimized method was performed with argon-saturated deionized water, under inert gas atmosphere, with a specific molar ratio of the precursor to reducing agent, and at a controlled reducing agent injection rate. Nanostructures produced in this manner were characterized by Transmission Electron Microscopy (TEM), Scanning Electron Microscopy-Energy Dispersive X-ray Spectroscopy (SEM-EDS), Selected Area Electron Diffraction (SAED), X-ray powder diffraction (XRD), and Infrared (IR) and ultraviolet-visible (UV-vis) spectroscopies.

4.1.2 Synthesis and Morphology Characterization

A series of trial reactions were performed to make elemental nickel nanoparticles from the reduction of nickel(II) chloride by sodium borohydride in aqueous medium. A summary of the experimental parameters and particle morphologies of these trial reactions can be found in Table 2. The first two trials evaluated the injection method for the additions of the reducing agent in ambient atmosphere, while maintaining at 1 hour reaction time and a Ni^{2+}:$NaBH_4$ molar ratio of 1:10. Trial 1 was performed by injecting $NaBH_4$ to $NiCl_2$ with a burette, and Trial 2 reversed the injecting chemicals and a siphon apparatus was used. Due to the fast addition rate and lack of control in addition, the nanostructures produced in this manner showed no control over the morphology or the reproducibility. Therefore, Trial 3 was performed by maintaining all reaction parameters constant as in Trial 1 but adding copper seed particles prior to the addition of $NaBH_4$. The inclusion of seed particles is a common method used to initiate particle nucleation in bottom-up synthesis processes for controlling the particle homogeneity and the morphology.

To overcome the above difficulties in the particle formation and reproducibility issues, the molar ratio between precursor and the reducing agent, and the addition method were adjusted in Trials 4-8. To minimize the particle oxidation during the reaction, all trial reactions were performed under inert atmosphere. During these experimental parameters optimization, a series of reactions were performed to identify an optimal molar ratio of the precursor to reducing agent, which was found to be 1:2. This molar ratio, inert atmosphere, and injection method were maintained throughout the rest of the trials, and this optimized method referred to as the "standard method". Trials 4 and 5 were performed with the standard method, but in Trial 5, Cu seed particles were included. No observable advantages

resulted from the inclusion of seed particles, so other parameters were tested. The repetitive

trials of reaction 6 were performed by changing the reaction time from 1 h to 2, 3, and 5 h.

Although these trials resulted in promising MNPs, reproducibility of nanostructures was

the greatest difficulty. Trial 8 describes the fully optimized and reproducible nickel

nanoparticle synthesis method, which avoids the undesirable formation of nickel oxide.

This was achieved by saturating the reaction solution with argon prior to the addition of

reducing agent, and purging the system with argon throughout the reaction, while

maintaining the injection rate at 0.11 mL/min over 45 minutes.

Table 2. Summary of Experimental Conditions and Nanostructures Morphologies.							
Trl #	Injection Method	Molar Ratio	Seed Particle (Y/N)	Reaction Time (hr)	Nanostructure Morphology	Ni conc. (%)	O conc. (%)
1[a]	Burette	1:10	N	1	Slightly aggregated spherical particles, 40±9 nm	56.9	32.4
2[a]	Siphon	1:10	N	1	Aggregated cotton ball-like structures, 49±12 nm	79.1	15.1
3[a]	Burette	1:10	Y	1	Aggregated spherical particles, 35±9 nm	77.8	18.4
4	Syringe	1:2	N	1	Well defined, aggregated spherical particles, 74±8 nm	89.8	7.17
5	Syringe	1:2	Y	1	Aggregated spherical particles, 23±2 nm	*	*
6	Syringe	1:2	N	1	Amorphous solid	*	*
	Syringe	1:2	N	2	Amorphous solid	*	*
	Syringe	1:2	N	3	Some particle-like structures and amorphous solid	*	*
	Syringe	1:2	N	5	Some particle-like structures and amorphous solid	*	*
8	Syringe	1:2	N	1	Well-defined slightly aggregated particles, 26±4 nm	95.6	4.23

[a]*Trials 1-3 were run under ambient conditions and 4-8 were performed under inert atmosphere.*

In all these trial reactions, particle formation was monitored using TEM. Figure 3 shows TEM images of Trial 1-5 after separating from the reaction mixture and re-dispersed in water. The particles produced from Trial 1 had an average diameter of 40±9 nm and were of consistent truncated shape and arranged in unordered aggregations (Figure 3 (a)). We speculate that the particle aggregation may be due to three primary factors. First, hydrogen gas bubbles were produced when $NaBH_4$ was added to water, which formed around the tip and inhibited consistent solution flow. Second, nickel is ferromagnetic, causing the particles to naturally coagulate. Third, NaCl is a side product of this reaction, which is a known to cause flocculation of solids in solution.[81] The size and monodispersed nature of the particles in Trial 1 is promising, but reproducibility was not achieved, likely due to uncontrolled injection. The elemental analysis obtained from EDS gave a composition of Ni 56.8%, and higher oxygen of 32.3%. Nickel readily oxidizes in air, so significant metal oxide formation is a result of the ambient atmosphere.

After several trial-and-error attempts to achieve consistent flow-rate, a siphon apparatus was designed in-house, and used to inject $NiCl_2$ into an open beaker of $NaBH_4$. Figure 1 (b) shows the morphological results of Trial 2. Particles aggregated similarly to Trial 1, but were slightly larger, 49±12 nm in diameter. Inconsistencies in morphology can again be attributed to rapid injection. EDS results were more promising for this trial. Ni concentration increased to 79.071% and oxygen more than halved to 15.070%. This reaction was run in ambient atmosphere, so it was surprising to observe such a marked decrease in nickel oxide formation. This decrease was likely due to switching the injected solution. Each drop of $NiCl_2$ solution was added directly to the $NaBH_4$ solution, and therefore the abundance of reducing agent reacting with Ni^{2+} atoms was greatly increased

32

compared to the previous trial. Additionally, $NiCl_2$ solution was added rapidly, so $NaBH_4$ had less time to decompose, and the reduction ability of $NaBH_4$ was higher in this case.

Particles produced to this point lacked the well-defined structure that is common to MNPs. Furthermore, highly ordered, crystalline particles are desirable for more finely tuned optical properties in many systems. In Trial 3, highly-ordered Cu nanoparticles, produced in-house,[82] were introduced to the reaction solution to initiate particle nucleation. Trial 3 was run with all reaction conditions maintained to that of Trial 1, excepting the inclusion of Cu seed particles, seen in Figure 3 (f), into the $NiCl_2$ solution. Based on the TEM image in Figure 3 (c) aggregated, spherical particles of 35±9 nm in diameter were formed with the similar particle composition of Ni and oxygen to that of in Trial 2, which is 77.8% and 18.4%, respectively. Here, the morphology of particles is largely unchanged from that of previous reactions.

Trials 4 and 5 introduced the standard method for the formation of MNPs, adapted from the work of Abeywickrama, et al.[82] These two trials maintained all parameters excepting the inclusion of Cu seed particles in Trial 5. In Figure 3 (d), the first spherical particles with well-defined edges, consistent morphology, and minimal oxidation were formed (89.8% Ni, 7.1% O). This is likely due to the controlled injection of reducing agent, and inert atmosphere. Comparatively, particles from Trial 5, shown in Figure 3 (e), exhibit the previously observed undefined edges, and cotton-like aggregations of solid. Particles are of consistent morphology, forming spheres of diameter 23±2 nm. The octahedral seed particles were not visible in the samples and this may be due to their low concentration.
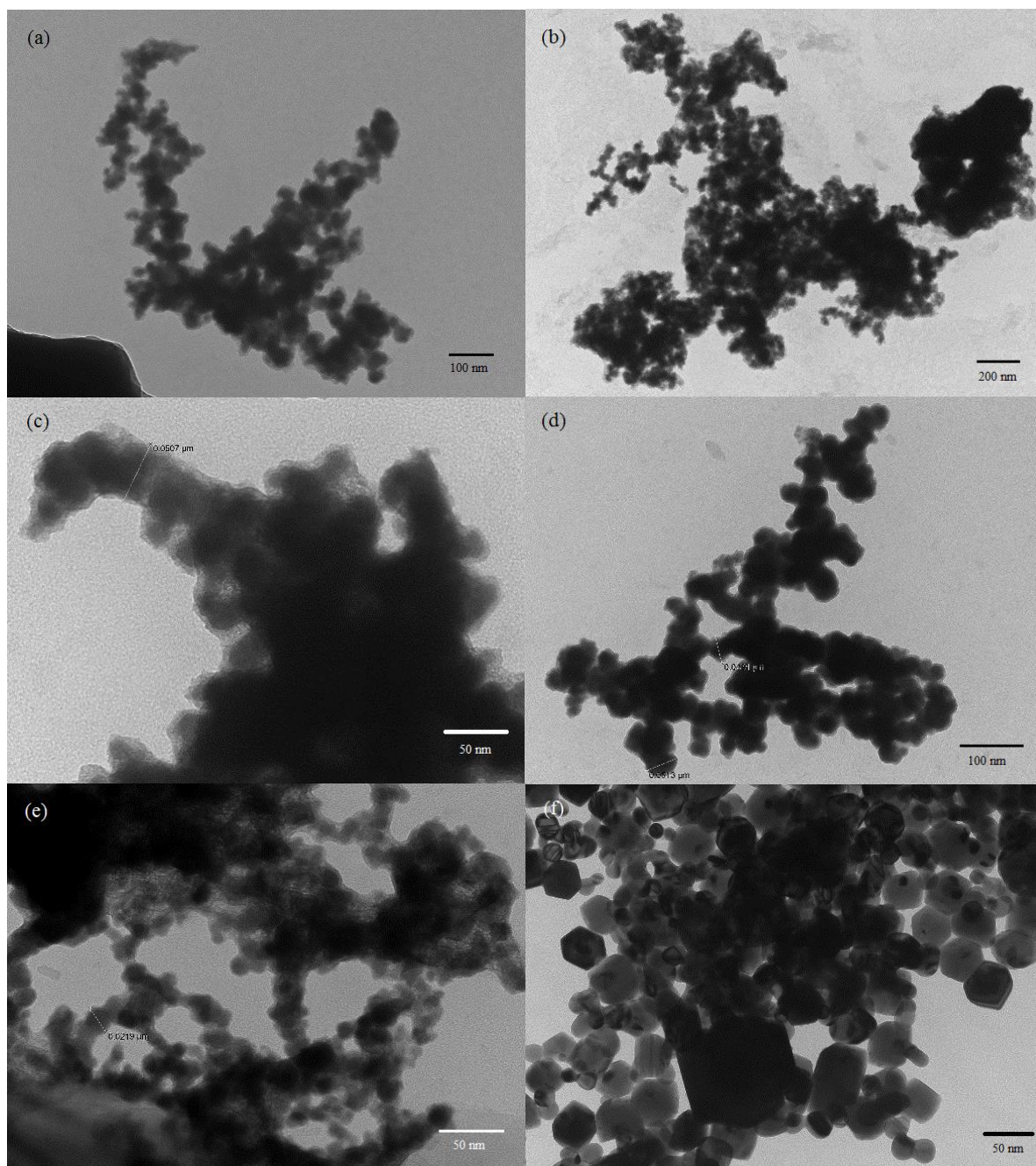
Figure 3. TEM images of Ni nanostructures from Trials 1-5 (a-e, respectively) taken from the samples after re-disperse in water. Image (f) is the Cu seed particles used in Trials 3 and 5.

From these trials, it can be determined that nickel MNPs of consistent and reproducible morphology cannot be formed under these conditions as evidenced by TEM and EDS analyses. It can also be concluded from these experiments that the inclusion of highly ordered Cu seed particles has no observable effect on the morphology of particles and does not accelerate nucleation of similarly ordered Ni nanoparticles, as was hypothesized. The greatest difficulty in Trials 1-5 was the lack of reproducibility. Furthermore, metal oxide formation was successfully minimized with inert atmosphere. It should be noted as well that EDS analyses were performed on samples, which had exposure to air. This fact could account for some oxygen in the sample.

From the previous trials, a standard method was developed, which exhibited promising nanoparticles, but the 1 hour reaction time was maintained throughout. In Trial 6, the effect of reaction time on particle morphology was evaluated. Figures 4 (a-d) show the morphology of structures formed from the standard reaction method at reaction times of 1, 2, 3, and 5 hours.

The structures observed in Figure 4 were formed under the same conditions as Trial 4, which exhibited the most promising morphologies thus far. The TEM images shown in Figure 4 of each hour's re-dispersed solid product demonstrate no clear trend with increasing reaction time. The amorphous solid shown in the 1 h sample demonstrates the irreproducible quality of particles under the same conditions as those of Trial 4, even with the standard method.

The image taken from 2 h reaction in Figure 4 (b) shows similar, but denser amorphous solid. The images in Figures 4 (c) and (d) of samples of 3 and 5 h reaction times, while

exhibiting more particle-like character than 1 and 2 h samples, still do not demonstrate the formation of individual particles as was observed previously.
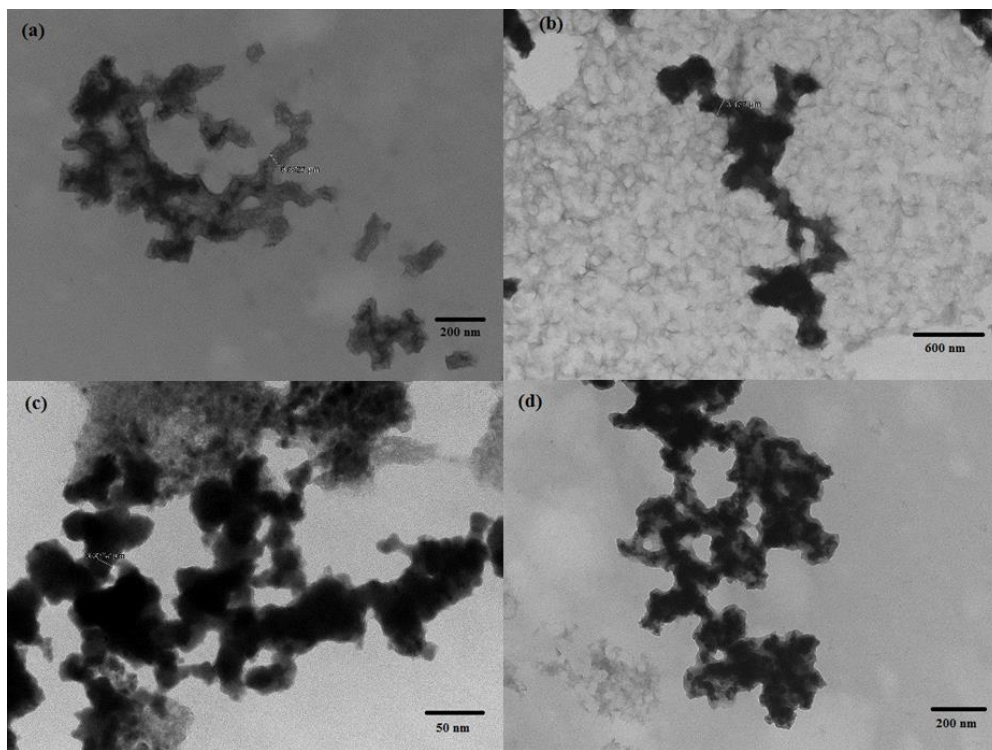
Figure 4. TEM images of Ni product from the standard method, run for 1 h (a), 2 h (b), 3 h (c), and 5 h (d).

From this experiment, it can be concluded that there is no reproducibility of the dense, well-defined spherical particles observed in Trial 4. It can also be determined that reaction time has no clear effect on nickel nanoparticle morphology, but only increases the density of the solid formed. This is likely due to the prolonged exposure of the product to NaCl in solution, promoting the aggregation of the solid.

In a final effort to synthesize reproducible nickel nanostructures with minimal oxide formation, each parameter that could be controlled in Trial 8 was identified and controlled if possible. This most optimized synthesis method maintained the reaction parameters of

the standard reaction, but minimized the product exposure to oxygen in air and dissolved in solution. Argon-saturated deionized water was used and argon was bubbled into the reaction solution throughout the entire reaction. Figure 5 shows the morphological results of this reaction method.
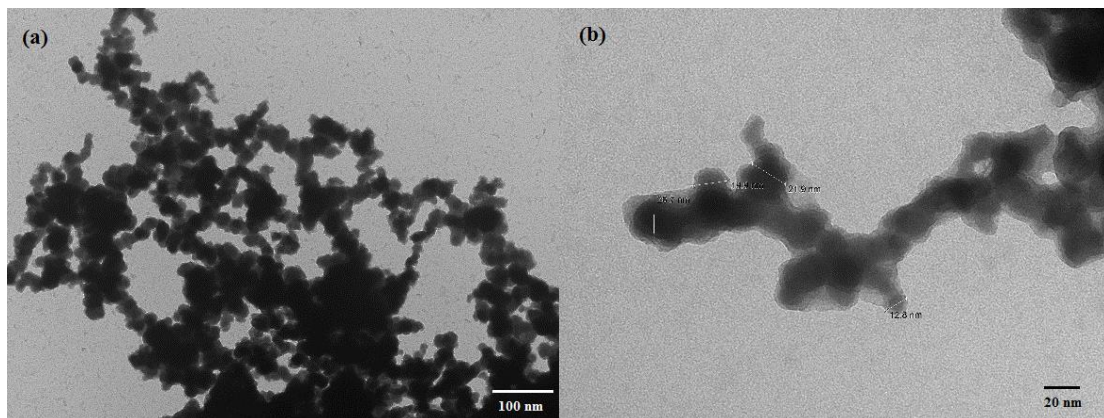
Figure 5. TEM images of Ni nanoparticles arranged in chain-like aggregates from Trial 8.

The particles produced from Trial 8 are well-defined, quasi-spherical particles of 15-25 nm diameter, arranged into chain-like aggregates. These particles are dense and were reproducible. Furthermore, EDS elemental analysis confirmed that significantly less oxide composition, with 95.5% Ni and 4.2% O. These values indicate that nickel MNPs were formed with the optimized solution conditions, with complete reduction and purification of nickel(II) chloride precursor. Figure 6 is an SEM image of the purified final nickel product. The notable observation here is the homogenous nature of the solid. There appears to be no structures or other solids present in this product—only aggregated particles. These results evidence that our water-ethanol purification method was effective in removing all unreacted reagents and impurities.
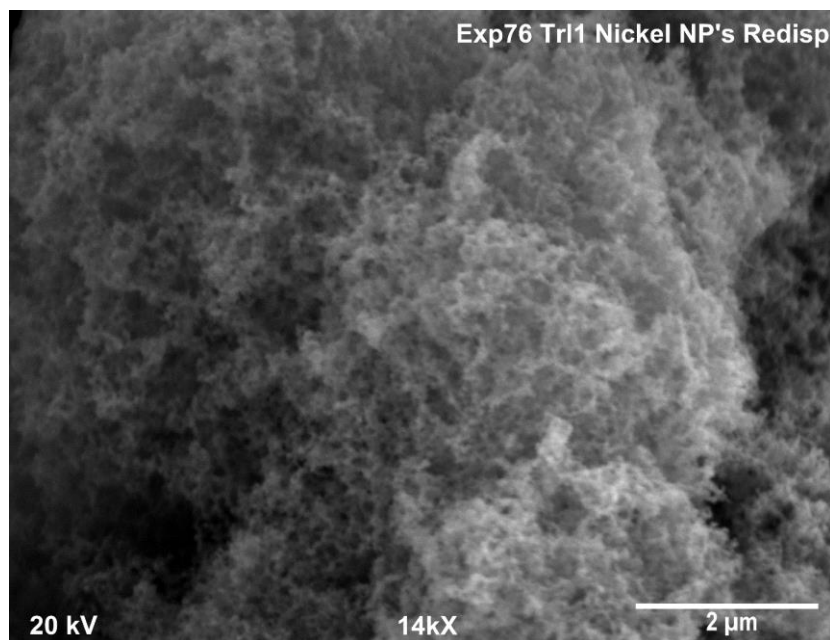
Figure 6. SEM image of Ni nanoparticles formed from Trial 8.

4.1.3 Powder XRD and SAED Analysis of Ni Nanostructures:

Because of the desirable properties of the particles formed from Trial 8, further characterization was performed including SAED, and XRD. Figure 7 (a) and (b) show the SAED diffraction pattern and the particles on which SAED was performed. There is no clear diffraction pattern, indicating that, either (1) the atoms within the particles are not arranged into a crystalline structure, or (2) the particles are too dense to properly diffract. It was also observed that the particles lose their structural integrity after exposure to the electron beam. The particles almost appear to melt, as is observable by the translucent shell around the particles in Figure 7 (b), not present in previous TEM images of this sample.
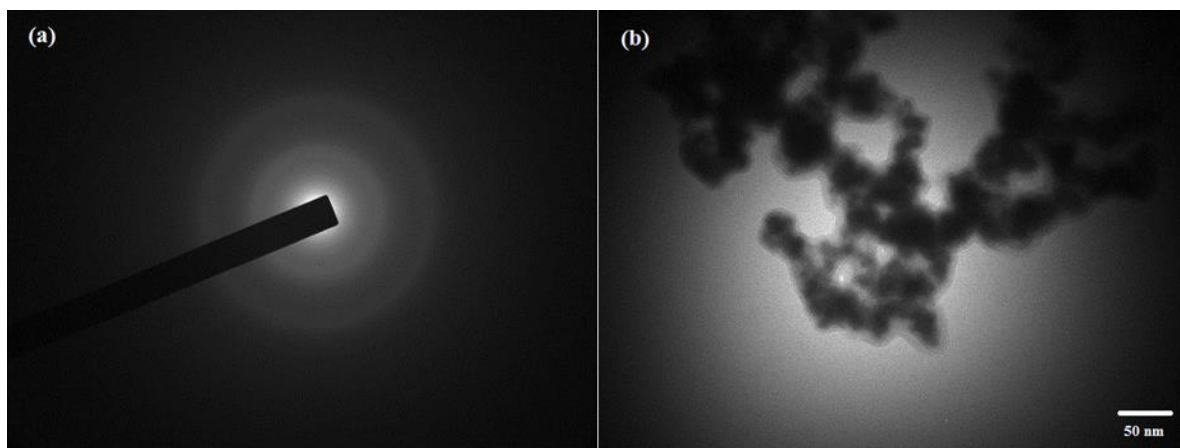
Figure 7. SAED diffraction pattern of Ni Nanostructures (a) and the structures analyzed (b).

Powder XRD was performed to further investigate the crystallinity of the Ni nanoparticles produced in Trial 8, and the diffraction pattern is shown in Figure 8. Previously reported XRD data reports peaks characteristic of Ni nanoparticles appearing near 2θ of 45°, 50°, and 75° consistent with face-centered cubic nickel. Although in our analysis, several broad peaks are observed at 2θ of 30° and 50°, with two sharp peaks at 2θ of 85° and 105°, there is no clear indication of well-defined packing pattern other than evidencing the crystallinity.
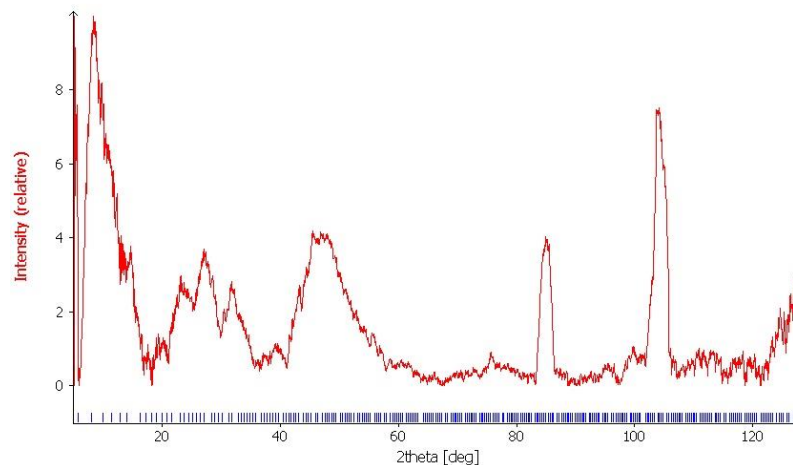
Figure 8. Powder XRD spectrum of Trial 8 Ni nanoparticles.

Overall, the results of the study described above indicate the sensitivity of aqueous-phase synthesis of elemental nickel nanostructures, produced without heat or capping agents. Reproducibility and significant oxide formation were the major challenges in these synthesis methods. These challenges were overcome with the removal of all possible oxygen present in the reaction. Final reproducible, monodispersed, crystalline nickel nanoparticles with insignificant oxide formation, and arranged in chain-like aggregates were produced with our optimized method. The method described here was then applied to zinc, iron, and iron-nickel alloy systems to determine versatility, described in the following sections.

4.2 Synthesis of Iron Nanoparticles using Optimized Experimental Parameters and Their Characterization

4.2.1 Overview

Iron is among the most abundant elements in Earth's crust. Finely divided iron nanoparticles have received attention due to their unique magnetic and catalytic properties at the nanoscale. Like the nickel structures described previously, their magnetic nature

makes them a viable candidate for application in diagnostics and catalysis. Unfortunately, physical synthesis methods are primarily employed, and require expensive equipment and large amounts of energy input. Some chemical reduction methods have been reported, but as was seen before, they are environmentally and economically not viable.[61]

The development of a synthesis method that can be used with a variety of transition metals is one of the primary goals of this research. This experiment is a test of the standard method's versatility with a series of different metal precursors. The standard method with optimized argon-saturated solution conditions, described in Trial 8, was performed with iron(II)chloride precursor. Particle characterization was performed by TEM, SEM-EDS, SAED, and UV-visible spectroscopy.

4.2.2 Iron Nanoparticle Synthesis and Characterization

Metal iron nanoparticles were synthesized by the standard method. Optimal reaction conditions are as follows: 1:2 molar ratio of Fe^{2+}: $NaBH_4$, under argon-saturated aqueous solution, room temperature, 0.11 mL/min injection rate over 45 min period, and 1 h reaction time. Here, samples were prepared for morphology analysis using TEM throughout the reaction time to monitor nanoparticle formation. The final product, purified washing multiple times with ethanol solution, and was also re-dispersed for analysis. A summary of the reaction conditions and corresponding morphological results is shown in Table 3.

Table 3. Summary of Fe Nanoparticle Morphology with Respect to the Reaction Time, Began After 45 min Injection Period.

Reaction Time (min)	Particle Morphology
0	Well-defined, non-dense, spherical particles in chains, 181±5 nm
15	Dense, aggregated particles in chains, 150±41 nm
30	Dense, aggregated particles in chains, 92±12 nm
60	Aggregated cotton-ball-like structures, No consistent size
Re-dispersed	Dense, well-defined aggregated spherical particles, 50±26 nm

Morphological results, analyzed by TEM, are presented in Figure 9, and demonstrate that Fe particle morphology varies greatly throughout this reaction process, but generally particles became smaller. At reaction time zero, chains of 181±5 nm spherical particles were present. These particles are not dense, as some light is passing through them, and they have well-defined edges. As the reaction progressed to 15 minutes, far denser, less-ordered, larger, and more polydispersed particles were present. The average diameter decreased to 150 nm, but the standard deviation increased to 41 nm.

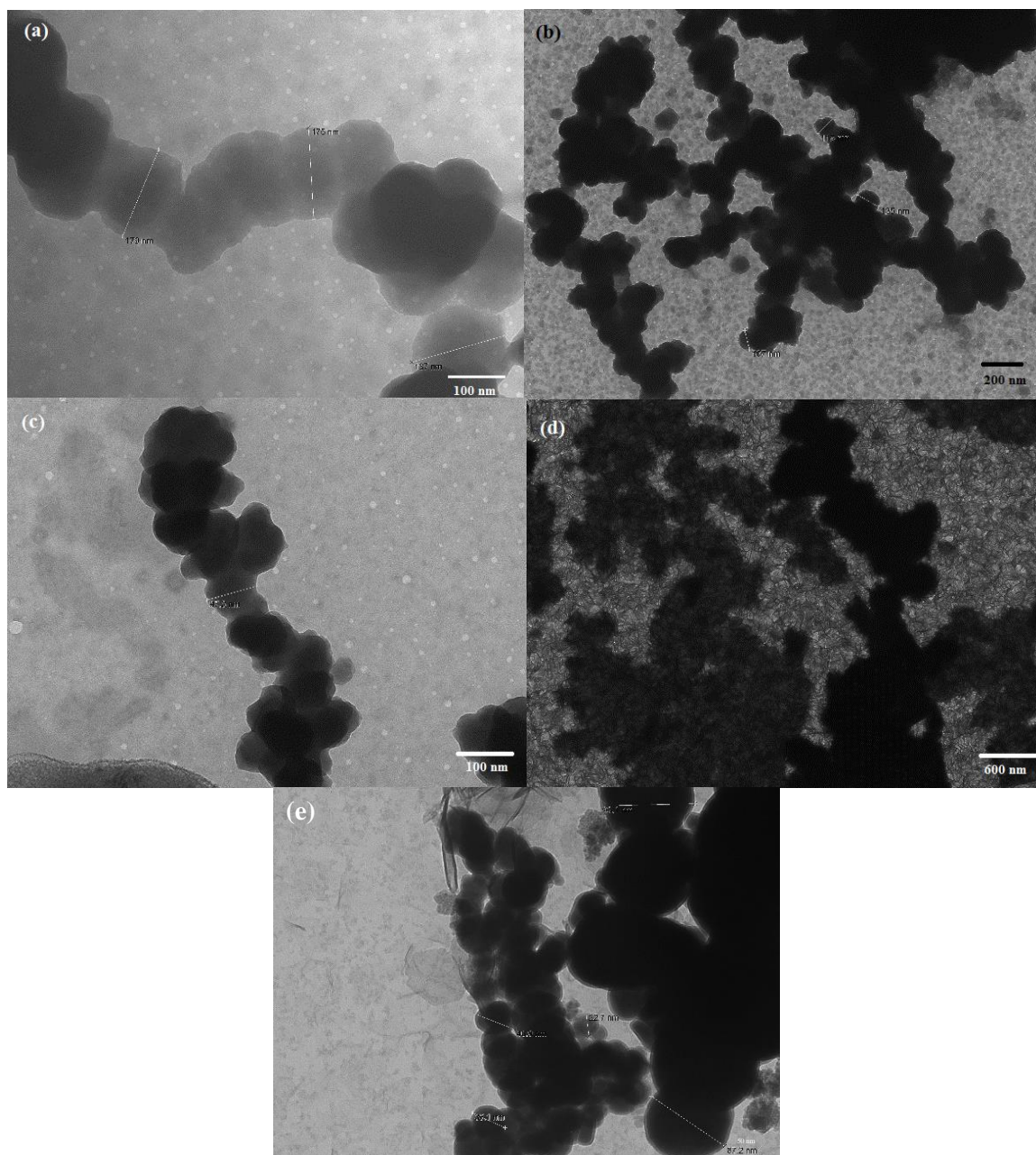Figure 9. TEM images of iron nanoparticles at 0 min (a), 15 min (b), 30 min (c), 60 min (d) and re-dispersed in ethanol (e).

At 30 minutes, particles maintained the dense aggregated nature similar to the 15-minute reaction time, but decreased substantially in diameter to 92 ± 12 nm. The particles produced in solution after 1 hour of reaction time were cotton ball-like structures, unordered in

aggregation, and discernable particles ranged from <100-600 nm in diameter. The final, purified, re-dispersed particles, shown in Figure 9(e), are dense, well-defined, spherical particles, which are moderately aggregated. Particles are polydispersed, though, with an average diameter of 50±26 nm. There were also impurities present in the final re-dispersed sample. One explanation for the lack of control in particle size distribution and morphology is iron's heightening reactivity at the nanoscale. Finely divided iron is so reactive that is it considered pyrophoric, and is often avoided by many researchers and explored so far in its oxide form.[61]

Elemental analysis showed Fe atomic percentage of 73.9%, but significant oxygen was present at 25.3%. This is due to iron's tendency to readily oxidize. It is likely that much of the iron oxide formed, was formed during the work-up process and during storing. There are also several different iron oxides that can form in air and are very stable, some including Fe_3O_4 and Fe_2O_3.[61]

Analysis of Fe nanoparticle crystallinity was performed by SAED of the re-dispersed sample. SAED results are presented in Figure 10. Upon close examination, a very dim diffraction pattern is visible in the SAED. This indicates that the particles likely have crystalline structure.
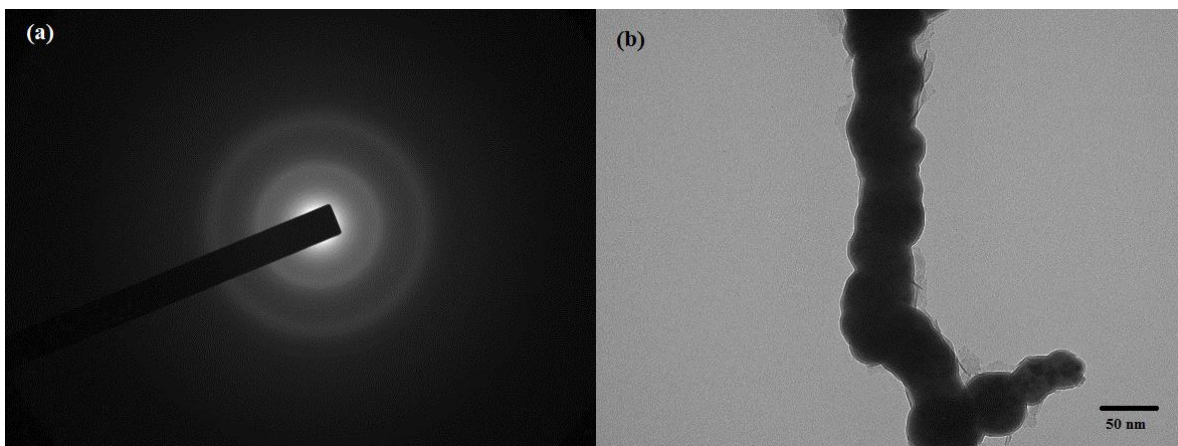
Figure 10. SAED pattern of Fe nanoparticles (a) and TEM image of sample area selected for diffraction (b).

A special property of iron is its ferromagnetism—a property that, in some reported cases, is enhanced at the nanoscale. As a simple demonstration of our Fe nanoparticle's magnetism, a photo was taken of the reaction solution after the 1-hour reaction time. Figure 11 shows the black solid Fe nanoparticles, which have flocked to the magnetic stir bar at the bottom of the reaction flask. This flocculation occurred within less than a minute after the stirring was stopped.
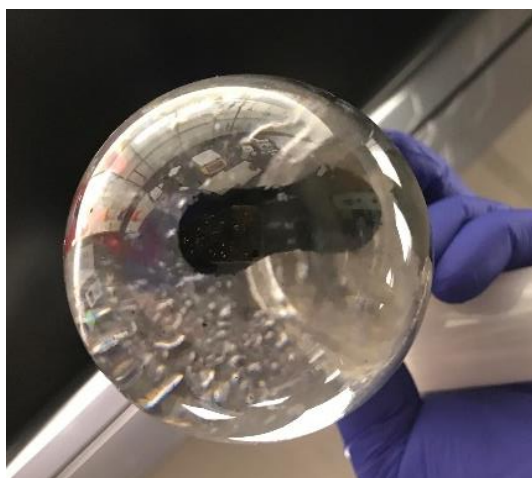
Figure 11. An image of Fe nanoparticles attracted to magnetic stir bar in the reaction solution.

Here, it is shown the standard method introduced and optimized for nickel nanoparticles could also be applied to an iron-based system. TEM morphological analysis demonstrated that, while particle morphology is inconsistent throughout the 1 h reaction time, the final particles are of the desired size and shape. As a trend, Fe nanoparticles became smaller throughout the reaction time. The most significant difficulty in this trial was preventing metal oxide formation. Without an air-stable capping agent, Fe nanostructures oxidize almost immediately, changing particle surface properties and therefore SPR associated with the material. Future work on the field will involve capping the particles with various organic capping agents and evaluating their optical and electrical properties, as well as their stability in air.

## 4.3 Zinc Oxide Nanoparticle Synthesis via Standard Method, Optimization, and Characterization

4.3.1 Overview

Zinc oxide is one of the most abundantly produced chemicals due to its wide commercial and chemical applications. The most common uses for ZnO are in cosmetics, paints, inks, and electronic, electrochemical, and electromechanical devices.[59] Due to these broad applications, ZnO is an attractive material in this research. ZnO is the third metal attempted in this series, evaluating the versatility of the standard method, developed with nickel, to synthesize transition MNPs. A general standard reaction method involves the reduction of metal(II) salt by the controlled injection of sodium borohydride in the aqueous phase and under inert atmosphere. This method is superior to common methods due to its environmental and economical low-impact, versatility, and simplicity. In the following reactions, reagent molar ratio and reaction time are varied to study their effect on ZnO

product morphology. Table 4 summarizes all ZnO trials. The nanostructures produced from these trials were characterized by TEM, SAED, and IR spectroscopy.

4.3.2 Synthesis and Characterization

The following trials are repetitions of the standard method, with modifications to evaluate reaction parameters. Standard reaction parameters are a 1:2 molar ratio of Zn^{2+}: $NaBH_4$, an argon-saturated environment, 0.11 mL/min injection rate over 45 min, and a 1 h reaction time. In early trials with zinc it was evident that zinc metal was not the primary product, and there was difficulty in forming any consistent and reproducible structures. Instead, the formation of zinc oxide was observed with these reaction conditions, and the scope of this series of trials was shifted. Early ZnO trials were performed similarly to those of nickel, but, here, a series of experiments were performed adjusting two reaction parameters, and evaluated the change in product morphology. Reagent molar ratio and reaction time were varied. Trials 10-14 were run with molar ratios of 1:1-1:5, respectively, each with samples prepared for TEM analysis throughout to monitor the reaction progress. Trial 10 includes samples from 0, 15, 30, 60, 120, and 180 min reaction time. Due to the generally unchanged morphology at the advanced time, Trials 11-14 were stopped at 60 minutes. Morphological analysis of all trials except Trial 10 resulted in inconsistent, amorphous, cotton-like solid. For this reason, the final ZnO trial (Trial 15) was performed at a 1:1 molar ratio, with all other reaction parameters maintained to that of Trial 10, while maintaining the pH at ≥10 of the solution. According to Xu, et al.,[59] ZnO nanostructures are best formed in a basic solution. Therefore, in Trial 15, the pH of the solution was increased to ≥10 by adding several drops of ammonium hydroxide before the addition of $NaBH_4$.

Table 4. Summary of ZnO trials with Modified standard method.			
Trial #	Molar Ratio Zn^{2+}: $NaBH_4$	Reaction time (min)	Nanostructure Morphology
10	1:1	0	Spherical particles, 70±20 nm
10	1:1	15	Amorphous solid
10	1:1	30	Amorphous solid
10	1:1	60	Spherical particle, 70±20 nm
10	1:1	120	Spherical particles, 52±9 nm
10	1:1	180	Amorphous solid
10	1:1	Re-dispersed	Amorphous solid
11	1:2	0	Amorphous solid
11	1:2	15	Amorphous solid
11	1:2	30	Amorphous solid
11	1:2	60	Amorphous solid
11	1:2	Re-dispersed	Amorphous solid
12	1:3	0	Amorphous solid
12	1:3	15	Amorphous solid
12	1:3	30	*
12	1:3	60	Amorphous solid
12	1:3	Re-dispersed	*
13	1:4	0	Amorphous solid
13	1:4	15	Amorphous solid
13	1:4	30	Amorphous solid
13	1:4	60	Amorphous solid
13	1:4	Re-dispersed	Amorphous solid
14	1:5	0	Amorphous solid
14	1:5	15	Amorphous solid
14	1:5	30	Amorphous solid
14	1:5	60	Amorphous solid
14	1:5	Re-dispersed	Amorphous solid
15	1:1	0	6-10 nm particle arranged into partially formed hexagonal plates, some crystalline solid
15	1:1	15	*
15	1:1	30	6-9 nm particle arranged into hexagonal plates
15	1:1	60	6-9 nm particle arranged into hexagonal plates
15	1:1	Re-dispersed	6-9 nm particle arranged into hexagonal plates
15	1:1	After filter	65 nm cubic nanostructures

Each sample was prepared for TEM analysis, but for the purposes of this discussion,

only images taken Trials 10 and 15 are included. All other morphological results, as shown

in Table 4, consist of amorphous, aggregates similar to that shown in the Figure 12 which are images of samples from 0, 15, 30, 60, 120, 180 min, and a re-dispersed product samples of Trials 10-14. Figure 12 (a) shows the morphology of ZnO nanoparticles at reaction time 0 min, after the complete addition of $NaBH_4$. Though sparse, spherical, 70 ± 19 nm particles were present, remain mostly unchanged after 60 minutes, and become smaller at 120 min, (Figure 12 (d) and (e), respectively). Particles were not present in samples analyzed at 15 min (Fig. 12 (b)), 30 min (Fig. 12 (c)), 180 min (Fig. 12 (f)), or the re-dispersed product sample (Fig. 12 (g)). These samples showed an inconsistent, aggregated, cotton-like solid, and even in samples where particles were present, this solid was abundant. It was unlikely that particles formed, disintegrated, and reformed throughout the reaction time. Particles were likely present, but simply too sparse across the sample, and were not observed. This experiment was repeated with all reaction conditions maintained, but reproducibility of the nanoparticles was not achieved. Only the same cotton-like solid was produced. This lack of reproducibility is likely due to uncontrolled and incompatible solution conditions for forming ZnO nanostructures. Trials 11-14 were performed at the varying Zn^{2+}: $NaBH_4$ molar ratios listed in Table 4, but only the same amorphous solid, similar to that shown in Figure 12, was produced. From these trials, it was evident that the solution conditions of the standard method were not suitable for ZnO nanostructure formation, and therefore further investigation was conducted.
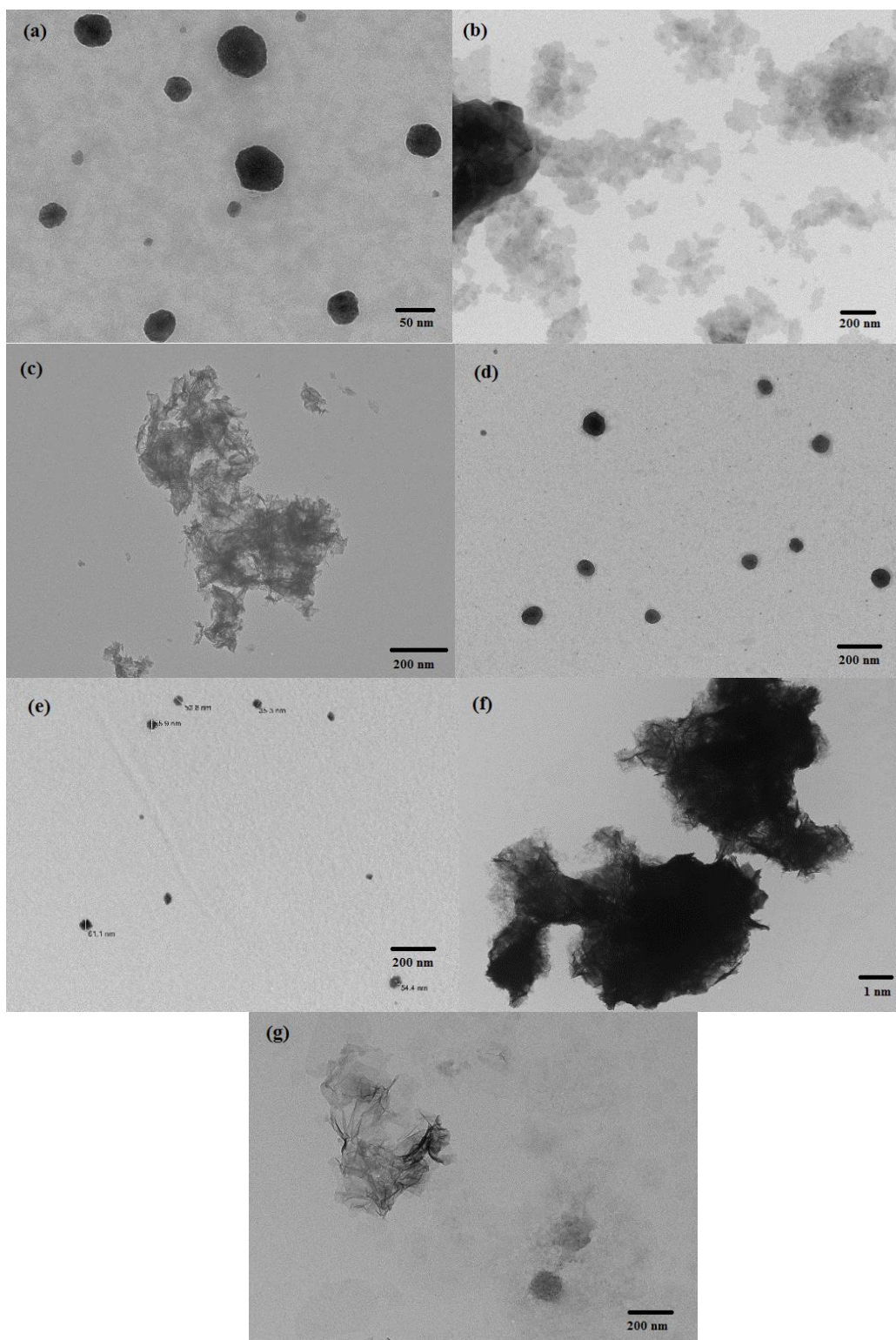
Figure 12. TEM images of ZnO nanostructures from Trial 10 at 0 min (a) 15 min (b) 30 min (c) 60 min (d) 120 min (e) 180 min (f) and the product re-dispersed in EtOH (g).

Trial 15 was performed at the same reaction conditions as Trial 10, excepting an elevated pH of approximately 10. TEM images of samples were taken at the same reaction times as previous reactions, and are shown in Figure 13. Here, we observed an interesting phenomenon unseen before in this work. Figure 13 (a) shows a mixture of irregular crystalline solid, and aggregates of smaller structures. As the reaction progressed, the aggregates became more ordered and demonstrated clear hexagonal structure. Upon closer examination, it was evident that the hexagonal structures were assembly of smaller nanoparticles. With the reaction time progress and after purification, as shown in Figure 13 (e), these particles and their hierarchical structures retain their morphology. The individual particles are 6-9 nm in diameter and appear to be spherical in geometry. Figure 13 (f) shows a high-magnification image of the particles, which are of consistent morphology and are arranged into single particle-thick layers.
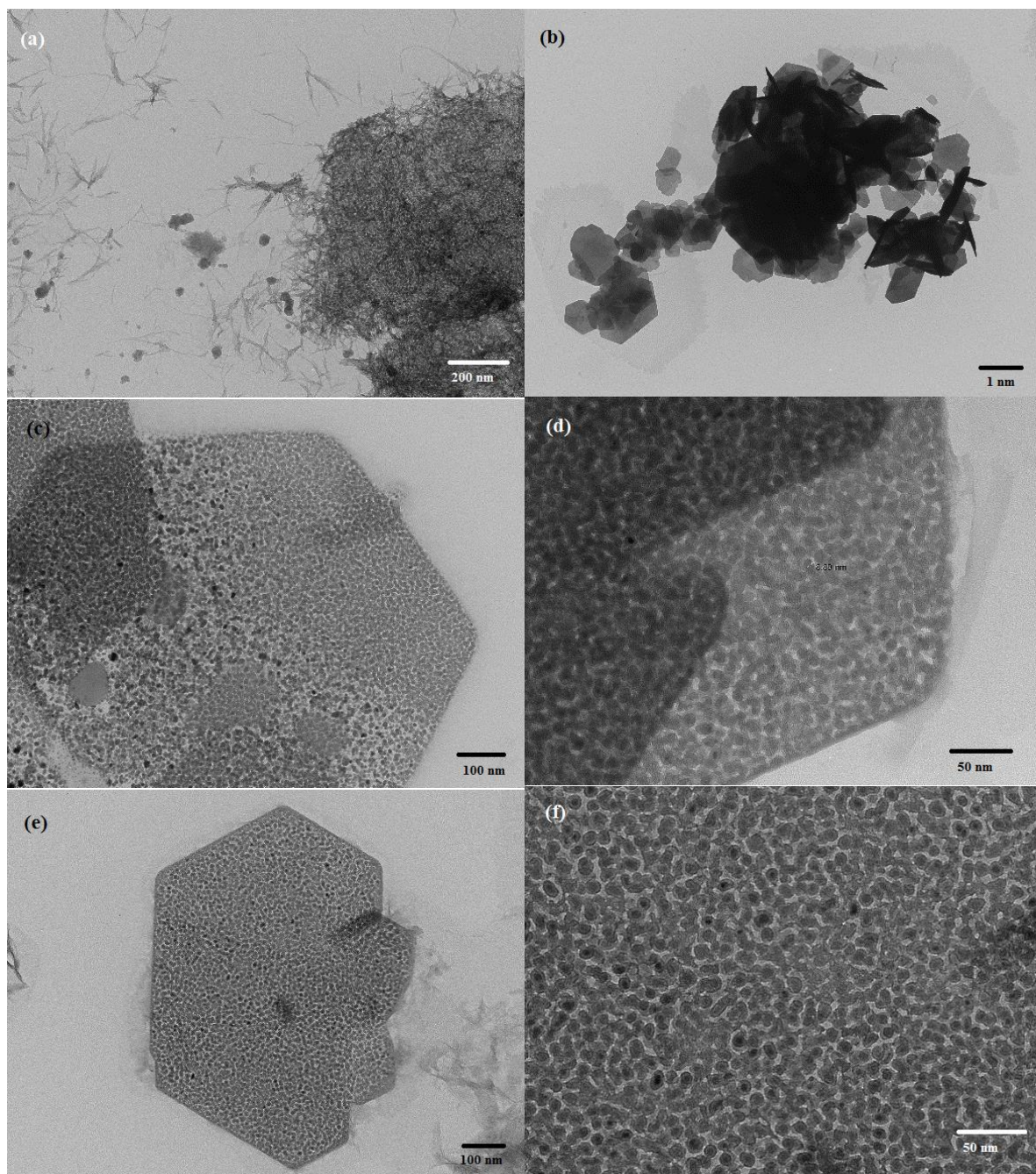
Figure 13. TEM images of ZnO structures from Trial 15 at 0 min (a), 15 min (b), 30 min (c), 60 min (d), re-dispersed product (e) and higher magnification re-dispersed product.

SAED was performed on these nanostructures to determine their crystallinity. Figure 14 shows the SAED diffraction pattern with the corresponding structures analyzed. The diffraction pattern indicates the polycrystalline nature of crystalline structures.
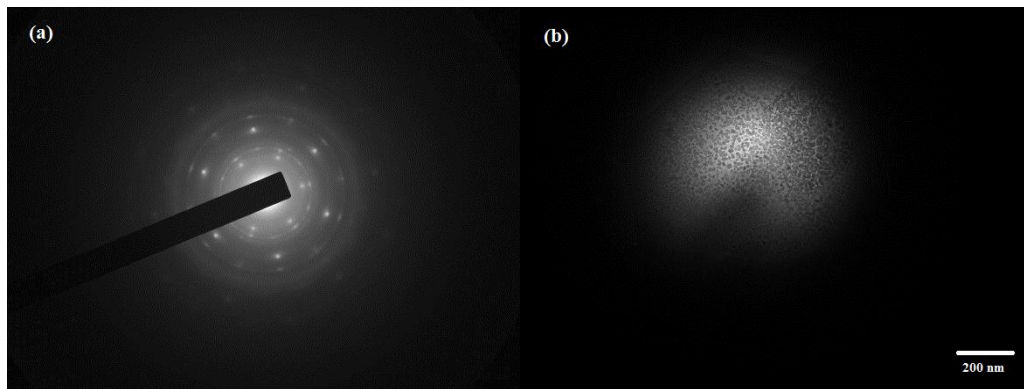

Figure 14. SAED diffraction pattern of Trial 15 ZnO nanostructures (a) and the corresponding particles (b).

To obtain a single particle crystal packing pattern, a small amount of the final dried product was re-dispersed in ethanol, passed through a 0.45 μm Millipore filter, and dropped onto a copper mesh grid for TEM imaging. Figure 15 shows these results along with the SAED diffraction pattern. There were no hexagonal plates present in this sample, but instead, particles 50-75 nm in diameter were present and also able to separate to single particles with less particle concentration. They also exhibited stability in the electron beam, unlike nickel nanoparticles discussed previously. This fact and the diffraction pattern present in the SAED image in Figure 15 confirmed the crystallinity of the particles present in the filtered product. Therefore, it can be concluded that several different structures are produced from the 1:1 molar ratio standard method synthesis of ZnO nanostructures in a basic solution. The primary nanoparticles produced from this method are of specific, and stable morphology, arranged in hierarchical hexagonal plates upon drying on the thin film.
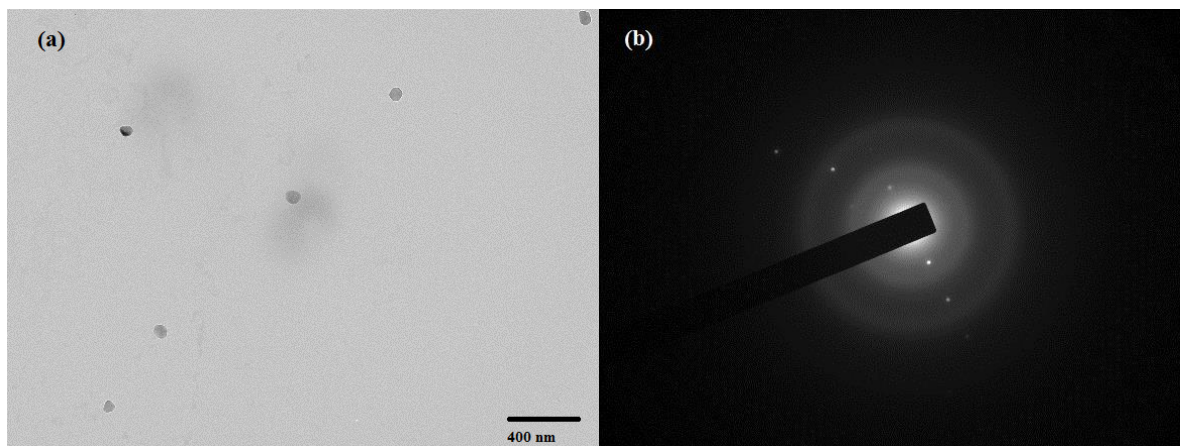
Figure 15. TEM Image (a) of particles present in solution after hexagonal plates were filtered out and (b) the corresponding SAED pattern of these particles.

IR spectroscopy was performed on the ZnO product produced from Trial 15 to determine the functionality present in the sample and is shown in Figure 16. The significant stretching is shown by the broad peak at 3430 cm^{-1}, indicative of O-H stretching due to adsorbed water, and some $Zn(OH)_2$ formation. The peak at 735 cm^{-1} is due to Zn-O stretching. Zn-O stretching peak is most commonly observed between 450-600 cm^{-1},[10,83] but this value varies depending on the particle morphology. It is possible that particles of our particular complex structure caused this higher wavenumber peak.

Figure 16. IR spectrum of ZnO product from Trial 15.

Overall, the formation of reproducible ZnO nanostructures was not successful using the standard synthesis method used for nickel and iron nanoparticle synthesis, even after adjusting reagent molar ratio and reaction time. Therefore, as indicated by the literature, a more compatible, basic solution condition was tested, and produced consistent, highly-ordered hierarchical ZnO nanostructures, self-assembled in solution.[59] Such structur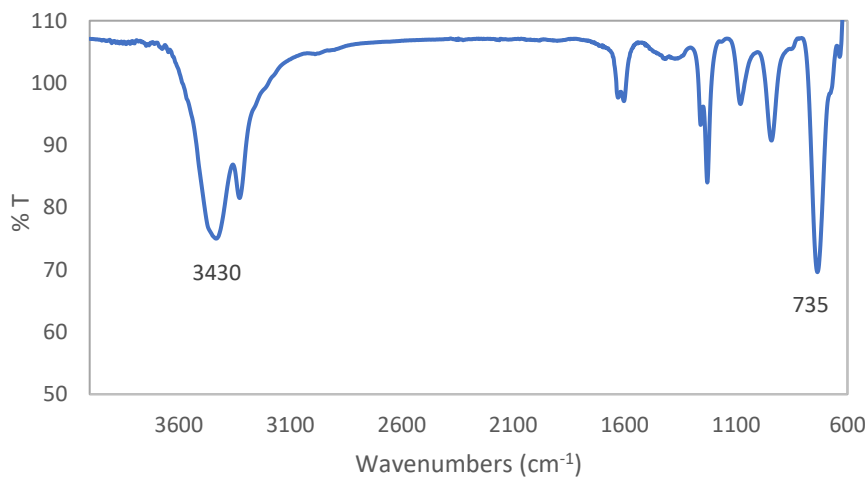es are highly advantageous when considering potential applications to electronic devices. The small particle size and their arrangement into the hexagonal pattern could facilitate efficient electron mobility in such a system.

4.4 Iron-Nickel Core-Shell and Alloy Nanostructures

4.4.1 Overview

This work shows that already broad properties of various nanostructures can be expanded by combining metals to form ordered and disordered bimetallic nanostructures. Additionally, nanoparticles of ferromagnetic materials have a wide number of applications including, but not limited to, diagnostics, computing, catalysis, and optical and electronic systems. The atoms within these nanostructures can take on several alloying patterns including mixed (unordered), sub-cluster separated, and core-shell morphology.[2] Here, the development of an environmentally benign synthesis method for iron-nickel alloy nanoparticles and their characterization is presented. The method was adapted from work by Zhou, et al.,[31] to fit our green synthesis standards by running the reaction in the aqueous phase, at room temperature, and with the mild reducing agent, NaBH4. Additional trials of each experiment were performed which included an organic polymer capping agent, polyvinylpyrrolidone (PVP). Capping agents are commonly included in MNP syntheses to control particle growth, aggregation, and to adjust optoelectrical properties. PVP is a

popular biocompatible, insulating, un-branched polymer capping agent, and its capping behavior could be indicative for the successful capping by other organic molecules. $FeNi_3$ particles described in this section were evaluated for their morphology, elemental composition, crystallinity, and optical properties by TEM, SEM-EDS, SAED, IR, and UV-vis spectroscopies.

4.3.2 $FeNi_3$ Nanoparticle Synthesis Procedure Optimization, Morphology, and Characterization

A series of trial reactions were performed to make iron-nickel alloy nanoparticles from the reduction of iron(II) chloride and nickel(II) chloride by sodium borohydride in aqueous medium. Trials were performed with and without PVP to evaluate particle grafting and morphology change in the presence of a capping agent. A summary of the experimental method, particle morphologies, and elemental composition of these trial reactions can be found in Table 5. The initial goal of these experiments was to form bimetallic core-shell alloy nanostructures. Trials 16 and 17 describe the first two attempts. These two trials were performed under the reaction conditions outlined by Zhou, et al.,[31] excepting NH_4OH used to raise the solution pH, $NaBH_4$ as the reducing agent, and 20 wt. % PVP as the capping agent in the latter trial. Multiple trials were performed of this reaction and TEM morphological analysis was performed on solution samples at 12 hours of reaction time and the product re-dispersed after purification with water and ethanol. Two repetitions of Trials 16 and 17 were performed, resulting in differing nanostructures with no reproducibility. Therefore a reaction with a more highly controlled environment was necessary. Trials 18 and 19 were performed maintaining all reaction conditions, but under complete argon gas saturation of the solution and reaction flask. This simple modification

was sufficient to produce monodispersed, reproducible particles, but neither a core-shell morphology nor PVP capping were observed in TEM images. Therefore, in the Trial 20, the effect of PVP concentration on particle morphology was performed at concentrations of 5, 10, 30, 40 and 50 wt. %. All other reaction conditions were maintained similar to Trial 18. Even after this concentration adjustment, there was still no clear capping of PVP to FeNi$_3$ alloy nanostructures.

To this point, since PVP capping was unsuccessful, other reaction pathways were explored. Trials 21 and 22 were performed under the Ar-saturated standard method described in previous sections, excepting a 20 min NaBH$_4$ injection period to try to reduce overall reaction time. For these trials, the molar ratios of reagents were the same as previous alloy experiments, and a 60 min reaction time was allowed after the complete addition of the reducing agent solution. PVP at 20 wt. % was added before NaBH$_4$ injection for Trial 22. Monodispersed particles with average diameter of 20 nm were produced and were assembled into chain-like aggregates. The PVP-capped reaction produced particles size roughly half of the uncapped product, and a translucent shell was present around particles. These results were able to reproducible.

In a final attempt to form alloy nanoparticles with a core-shell morphology, a sequential reduction method was performed under further modified Zhou[31] reaction conditions. We hypothesized that the reduction of one metal would form a core and the second metal would form a shell around it after the sequential reduction. First, FeCl$_2$ was reduced with half of the original NaBH$_4$ mass, under Ar-saturated conditions, for 12 hours. After this reaction period, a small amount of from the reaction product was isolated for

analysis, and the $NiCl_2$ and remaining $NaBH_4$ was added to the solution to react for another

12 hours.

Trial #	Method	PVP Y/N (wt %)	Reaction Time (h)	Particle Morphology	Fe Conc. (%)	Ni Conc. (%)	O Conc. (%)	C Conc. (%)
	Table 5. Summary of Iron-Nickel Alloy Synthesis Methods.							
16	Modified Zhou	N	12	Round, cotton-like aggregated particles, 35±8 nm	5.51	35.2	35.7	23.2
17	Modified Zhou	Y (20%)	12	Amorphous cotton-like aggregates	6.78	14.7	37.0	41.3
18	Modified Zhou, Ar-saturated	N	12	Spherical particles, 64±19 nm	8.95	36.6	54.0	*
19	Modified Zhou, Ar-saturated	Y (20%)	12	Spherical particles, 35±14 nm	10.5	37.0	51.5	*
20	Modified Zhou, varying PVP	Y (5%)	12	Spherical particles, 47±6 nm	*	*	*	*
20	Modified Zhou, varying PVP	Y (10%)	12	Spherical particles, 46±9 nm	*	*	*	*
20	Modified Zhou, varying PVP	Y (30%)	12	Spherical particles, 32±4 nm	*	*	*	*
20	Modified Zhou, varying PVP	Y (40%)	12	Spherical particles 29±5 nm	*	*	*	*
20	Modified Zhou, varying PVP	Y (50%)	12	Spherical particles, 32±4 nm	*	*	*	*
21	Standard	N	1	Particles in chain-like aggregates, 20±3 nm	9.10	60.1	29.1	*
22	Standard	Y (20%)	1	Capped aggregated particles 11±2 nm	6.63	24.2	65.3	*
23	Sequential Reduction, Fe "Core"	N	12	Spherical particles, 120±20 nm	18.9	0.179	64.5	*
23	Sequential Reduction with Ni "shell"	N	12	Polydispersed, aggregated particles, smaller with 6.8±0.7 nm diameter	5.06	39.0	51.8	*

Particle morphology of all trials was determined by TEM taking samples directly from the solution at the end of the reaction time and products after purification, and re-dispersed in ethanol. An example of particle morphology from Trials 16 and 17 are shown in Figure 17.

Figure 17. TEM images of (a) Reaction solution FeNi3 (b) Reaction solution $FeNi_3$-PVP (c) Re-dispersed $FeNi_3$ in EtOH (d) Re-dispersed $FeNi_3$-PVP in EtOH.

In these series of trial reactions, the Trial 16 reaction solution shows plate-like structures approximately 500 nm in size, but which disappear upon purification in the re-dispersed sample. The final product showed cotton ball-like particles, 35±8 nm in diameter. The reaction solution in Trial 17 showed globular structures approximately 800 nm in diameter, but similarly to Trial 16, these structures disappeared throughout the workup. In this

example, random structured solid was produced. These inconsistent structures, and those produced in the repeated trials, are a result of uncontrolled reaction parameters. In early trials, the solution overflowed upon the addition of $NaBH_4$, so subsequent optimization experiments were performed. In all these trials, it was observed that morphologies of nanostructures produced in the solution were different from the nanostructures separated from the reaction mixture.

To determine the elemental composition of the product, EDS analysis was also performed. The composition of Fe to Ni were present in an approximately 1:7 ratio, with 35.7% of O and 23.2% of C. Upon the addition of PVP to the reaction, the C content has increased up to ~20%, oxygen remained nearly unchanged, Ni nearly halved and Fe increased 1.27%. The significant increase in C is expected due to the addition of an organic material, but the oxygen values are too high to confirm the formation of elemental metals, rather than metal oxides.

Trials 18 and 19 were performed after multiple different experiments to optimize the reaction conditions. The TEM images shown in Figure 18 compare the morphology of uncapped and capped alloy nanoparticles. Similar to the previous trial, the reaction solution structures are not the same as the purified product, but are different in a consistent way. Both Trial 18 and 19 reaction solutions exhibit unordered aggregates that later condense to individual spherical nanostructures With the addition of PVP the diameter of the nanoparticles decreases from 64±19 nm to 35±14 nm, but there was no visible polymer coating around the particles that confirm the successful grafting of PVP on to the surface. However, these results clearly evidence that addition of PVP has clear effect on controlling

the particle size and confirming PVP acts as a surfactant rather than a capping agent in this case.
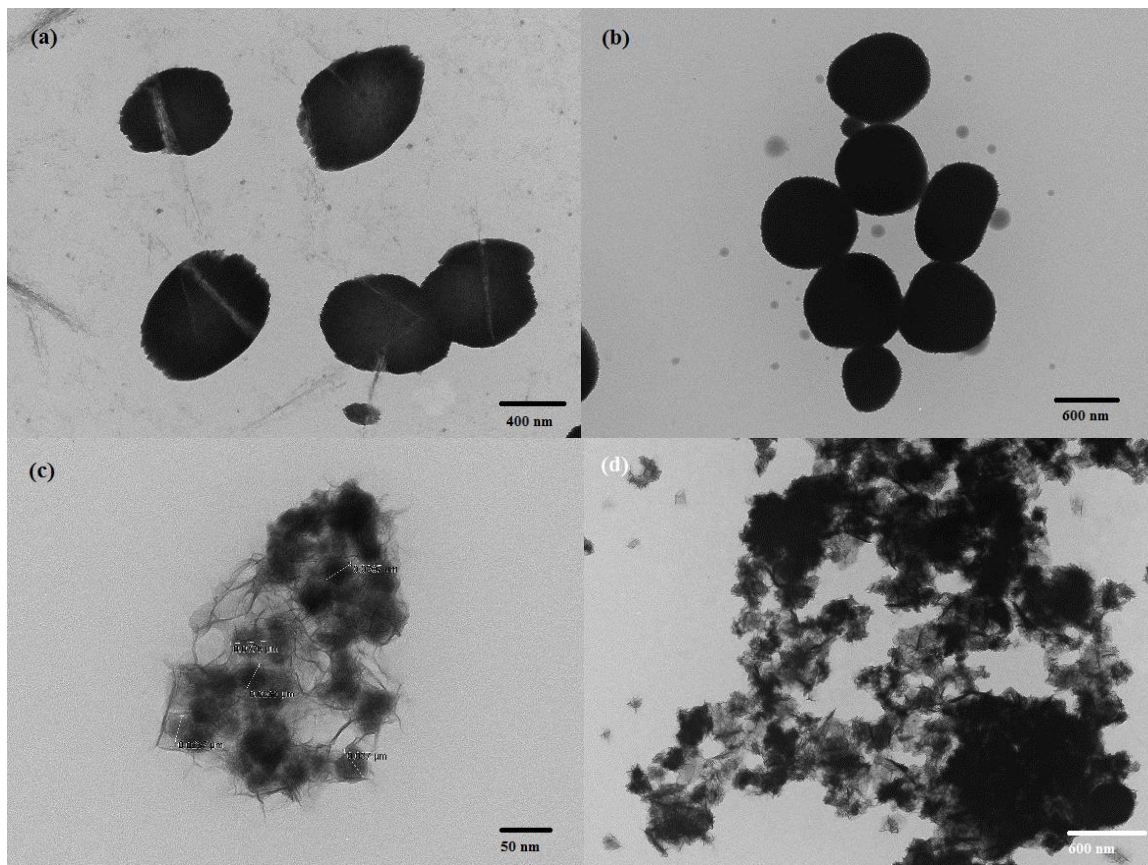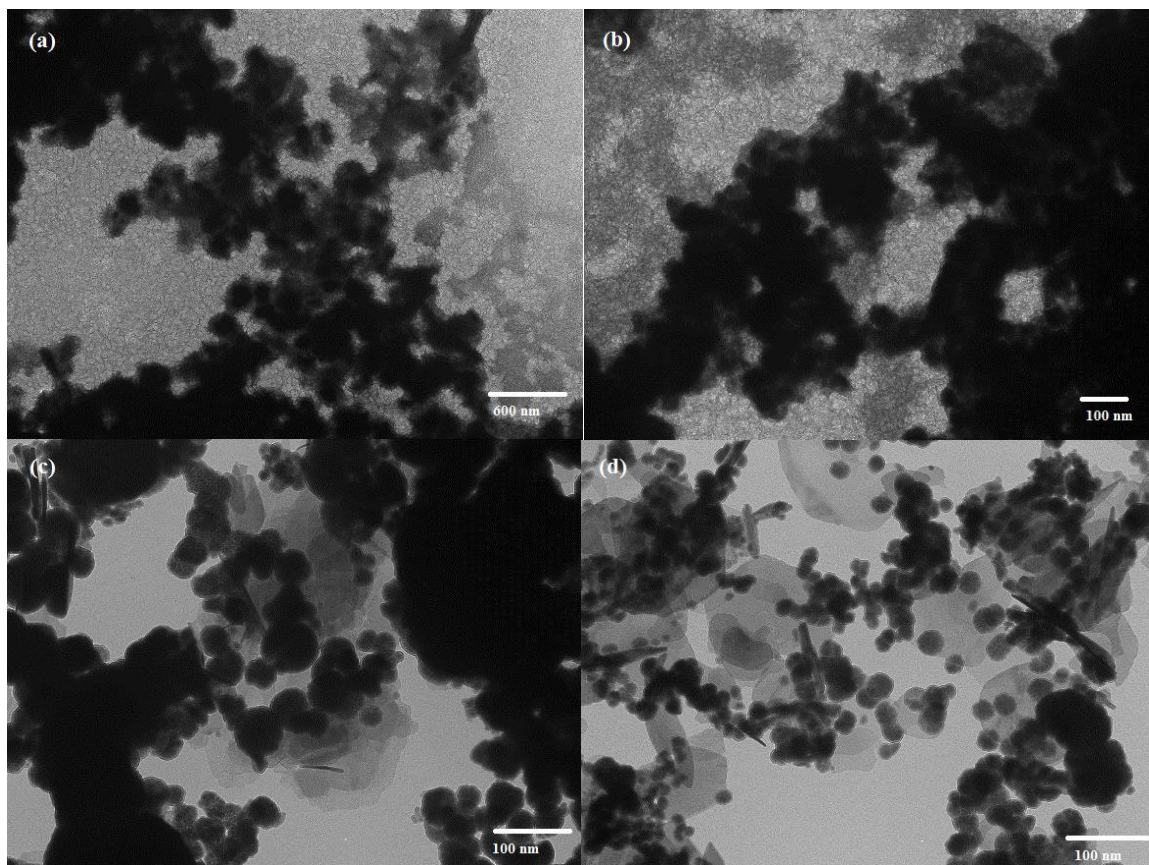

Figure 18. TEM images of (a) Reaction solution $FeNi_3$ (b) Reaction solution $FeNi_3$-PVP (c) Re-dispersed $FeNi_3$ in EtOH (d) Re-dispersed $FeNi_3$-PVP in EtOH.

A major difficulty in this synthesis process was metal oxide formation, as both iron and nickel both readily oxidize in air. Throughout the optimization of the nickel nanoparticle synthesis, there was a marked decrease in oxygen present in the product formed after the solution and reaction flask was purged with Ar gas. Here, after performing the same Ar saturation, there was no decrease in oxygen. In fact, the atomic percentage of oxygen remained almost unchanged with the % oxygen content of 54.0 and 51.5% in Trials

18 and 19, respectively. This clearly confirmed that avoiding metal oxide formation during the reaction and purification process is difficult and challenging.

Particle crystallinity was evaluated by performing SAED on the particles produced from Trials 18 and 19. Figure 19 shows the SAED results of both capped and uncapped particles along with their TEM images.
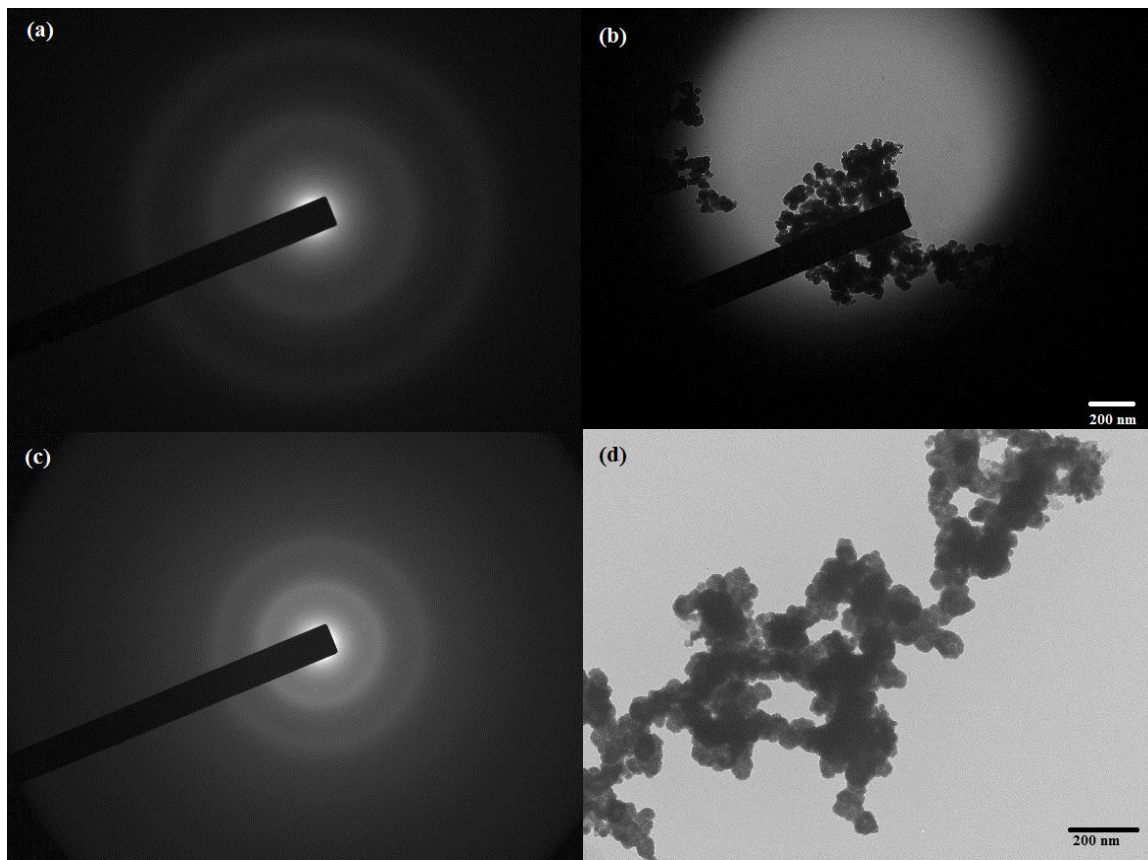

Figure 19. SAED patterns with their reference images for Trials 18 (a) and (b), and Trial 19 (c) and (d).

There is no diffraction pattern present in either sample, potentially indicating that the particles are not crystalline in nature, but these results could also be due to either particles being too dense or oxide layer coated around the particles, which prevents the diffraction.

Additionally, it was observed that the particles were not stable in the electron beam. In fact, they appeared to melt with prolonged exposure.

To evaluate the presence of PVP in the product, IR analysis was performed on capped and uncapped particles, and pure PVP. If the capping agent was present in capped particles, characteristic peaks from the PVP spectra would also be present in the $FeNi_3$-PVP spectra and not present in the $FeNi_3$ spectra. Shown in Figure 20, characteristic carbonyl stretching was present in the PVP spectrum at 1653 cm^{-1}, and the $FeNi_3$-PVP spectra shows a subtle peak at the same wavenumber.
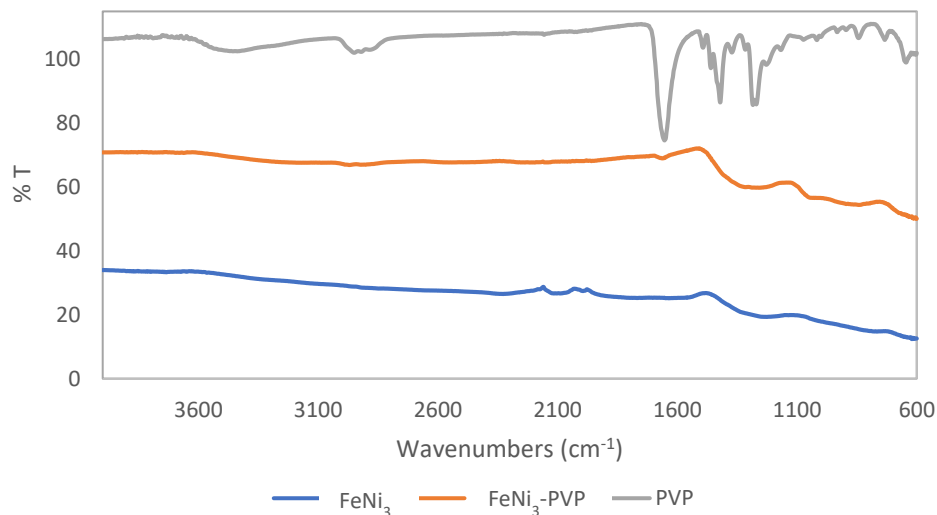
Figure 20. IR spectra of Trials 18 and 19 and PVP.

The lack of intensity of this peak indicates that very little PVP is present in this sample, likely only as contamination rather than PVP capped to particles. This peak disappears entirely in the uncapped $FeNi_3$ spectrum, as expected. Similar stretching is also shown in the fingerprint region of the spectra for both metal samples. UV-vis spectroscopy was performed on the samples in an ethanol solvent, but no absorption peaks were detected and

further evidences that presence of oxide layer around metal alloys, which prevents the surface plasma resonance of the metal surface.

4.4.3 Effect of PVP Concentration on Particle Morphology

In previous experiments, the concentration of capping agent was held constant, but in Trial 20 the synthesis of PVP-grafted $FeNi_3$ alloy nanoparticles was attempted by varying PVP concentration while maintaining all other reaction conditions as in Trial 19. Morphologies and particle formation for each trial were analyzed by TEM and are shown in Figure 21. The appearance of the particles is generally unchanged from the particles in Trial 19. There are somewhat aggregated, spherical particles without a clear-capped shell. Additionally, there is a subtle decrease in the average diameter with the increase of PVP concentration. According to these analyses, with the wide range of PVP concentrations evaluated, it is unlikely that a PVP shell will form around nanoparticles with the modified Zhou method presented here. A more in-depth investigation should be performed in future work adjusting the sequence of reagent addition and capping agent structure. As further explanation for this behavior, comparing experiments that included PVP reacted more violently than those without. $NaBH_4$ produces significant effervescence when reducing metals, but with PVP inclusion, $NaBH_4$ addition had to be performed carefully to prevent overflow. In solution, $NaBH_4$ decomposes producing H_2 gas. This reaction is generally slow, and is slower yet in a basic solution, but more reactive in an acidic environment. PVP has a slightly acidic character, likely causing $NaBH_4$ to decompose more rapidly. This more rapid reduction adjusted the solution conditions and particle grafting by PVP is shown to not be favorable in these conditions. Adjusting the pH of the solution in future work could be a viable option to create a better capping environment.
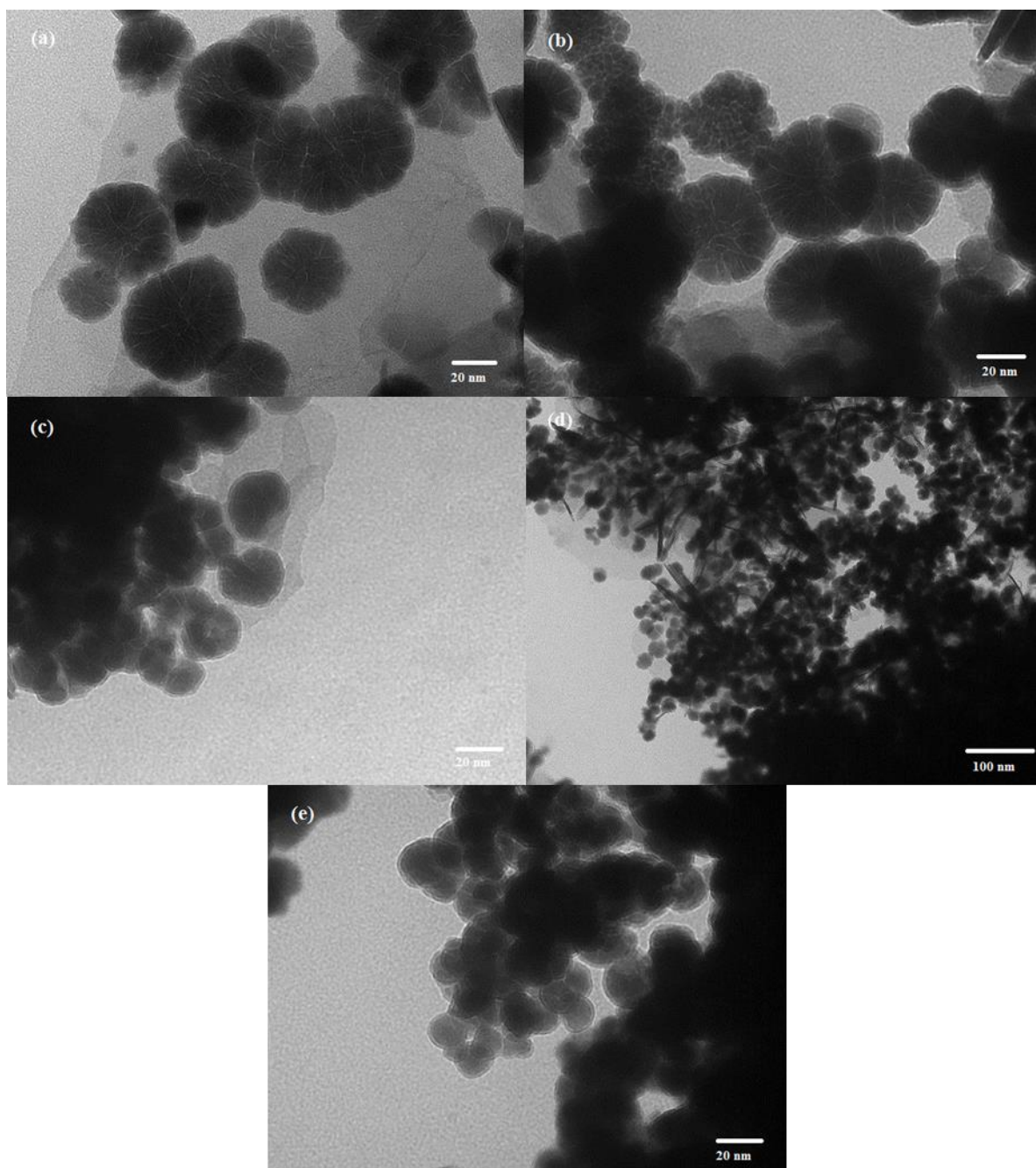
Figure 21. TEM Images of (a) 5% (b) 10% (c) 30% (d) 40%) and (e) 50% PVP

4.4.4 Standard Method Synthesis of Capped and Uncapped FeNi₃ Nanostructures

One of the major advantages to our standard method for MNP synthesis is its versatility for a wide range of transition metals. To further confirm its versatility, this

method was applied to make capped and uncapped bimetallic $FeNi_3$ system following the similar parameters as in Trial 18 and 19. The only parameter, which deviated from the standard method described previously is the injection time of the reducing agent and was maintained at 20 minute. Morphological analysis was performed on the products from this synthesis method without and with PVP, Trials 21 and 22, and is shown in Figure 22.
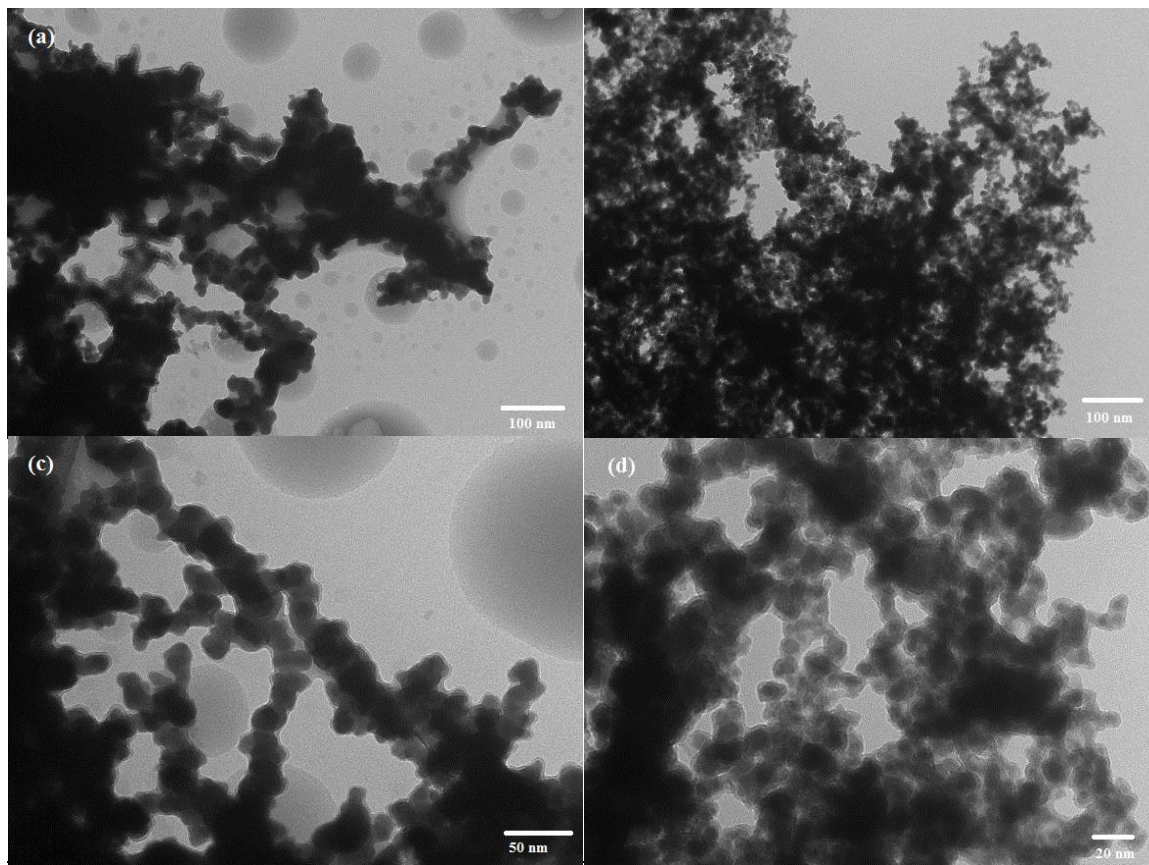
Figure 22. TEM images of Trial 21 (a) and Trial 22 (b) at low magnification and at high magnification (c) and (d), respectively.

Trial 21 resulted particles in chain-like aggregates with an average diameter of 20±3 nm. These particles do not exhibit individual spherical morphology. Instead they are generally round and somewhat inconsistent in shape, as is better seen in the higher magnification image in Figure 22 (c). $FeNi_3$-PVP particles in Figure 22 (b) and (d) are approximately half

the diameter of Trial 21 particles, at 11±2 nm. In the higher magnification image (Figure 22 (d)), it is evident that PVP has capped by the translucent coating around the particles that is not present in the corresponding uncapped particle sample. Aggregation of the particles follows a trend uncharacteristic of such capped structures.

SAED was performed on these samples to determine the crystallinity of the particles. Figure 23 shows the SAED pattern samples from Trial 21 and 22. Neither sample shows a diffraction pattern. This could indicate that the particles are not crystalline in nature, but these results could be due to high particle density or the formation of a metal oxide layer around the particles, preventing diffraction.
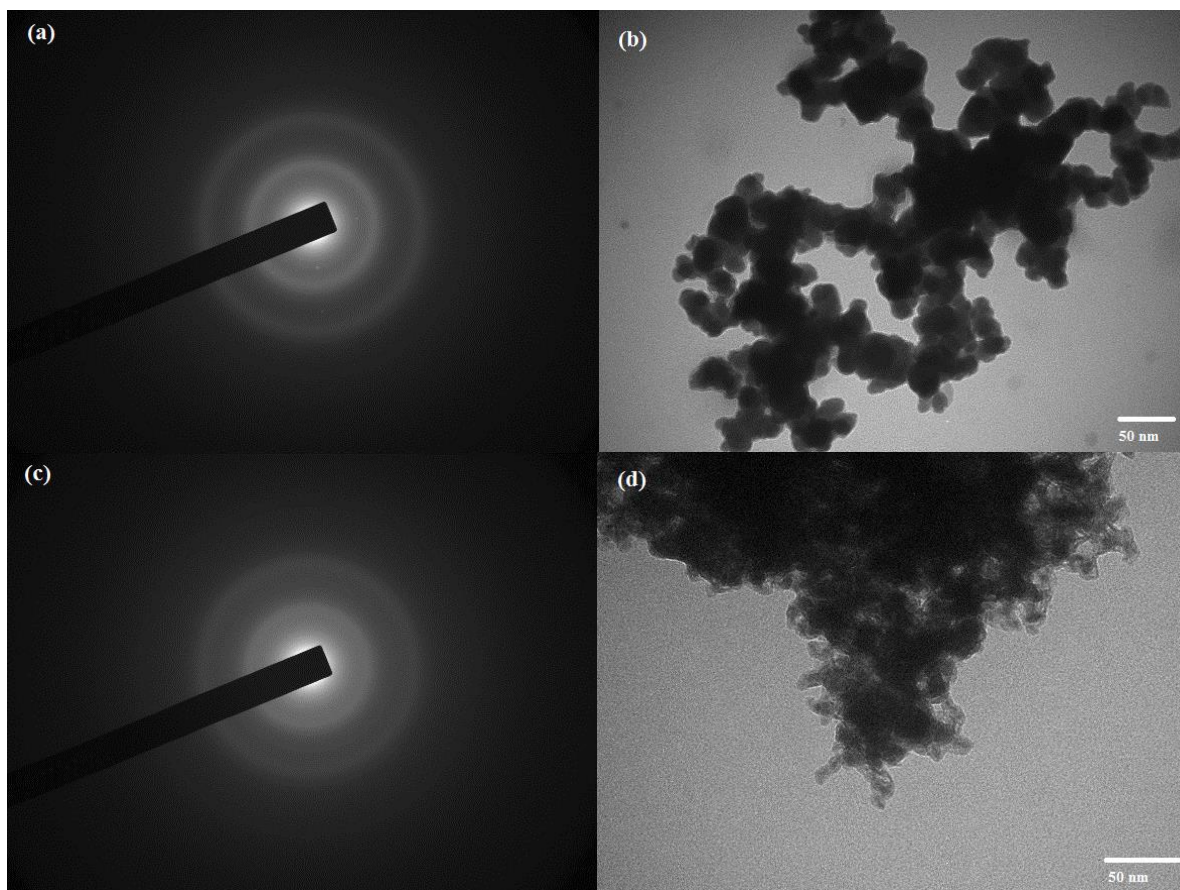

Figure 23. SAED patterns of Trial 21 (a) and Trial 22 (c) with their respective reference images.

IR and UV-vis spectroscopies were performed on the samples of Trials 21 and 22 in an effort to confirm PVP grafting that was observed in morphological analysis and to determine the SPR absorption. Neither analyses exhibited peaks in the IR or UV-vis region. From these analyses, it cannot be determined that particle grafting was successful and the particles do not exhibit SPR.

4.4.5 FeNi$_3$ Core-shell Nanoparticle Synthesis via Sequential Reduction

In a final effort to synthesize iron-nickel ANPs with a core-shell configuration, a sequential reduction process was performed. Here, iron nanoparticles were reduced to form an iron core in reaction conditions similar to those in Trial 19. After 12 hours of reaction time and Fe nanoparticle analysis, Ni was subsequently reduced in the same solution to form a shell. TEM analysis was performed on the iron sample and the final product re-dispersed in ethanol, shown in Figure 24. Three trials of this reaction were repeated; resulting in widely varied morphological results. The images included are of the particles of the most abundant and consistent morphology. Iron core particles were of spherical morphology, moderately aggregated, and had an average diameter of 129±16 nm. After sequential reduction, the particles present were widely varied, but extremely small structures that were not present in the iron core sample were consistent across the entire sample. These particles were 6.0±0.7 nm in diameter and arranged into many different aggregate geometries. In some cases, the small particles appeared to arrange around what is assumed to be the larger iron particles. Other formed single-particle thick round plates of particles, and randomly arranged particles.

Elemental analysis was performed on the iron core intermediate and the final iron-nickel product. The values listed in Table 4 show a rather low Fe concentration of 18.9%

and high 64.5% oxygen concentration. These data indicate significant metal oxide formation. The <1% Ni concentration is negligible. After the full reaction with Ni the product was 39.0% Ni, 5.06% Fe, and 51.8% O. This ratio of Ni to Fe is expected, but O, again, is too high to confirm elemental metal formation and not metal oxide.
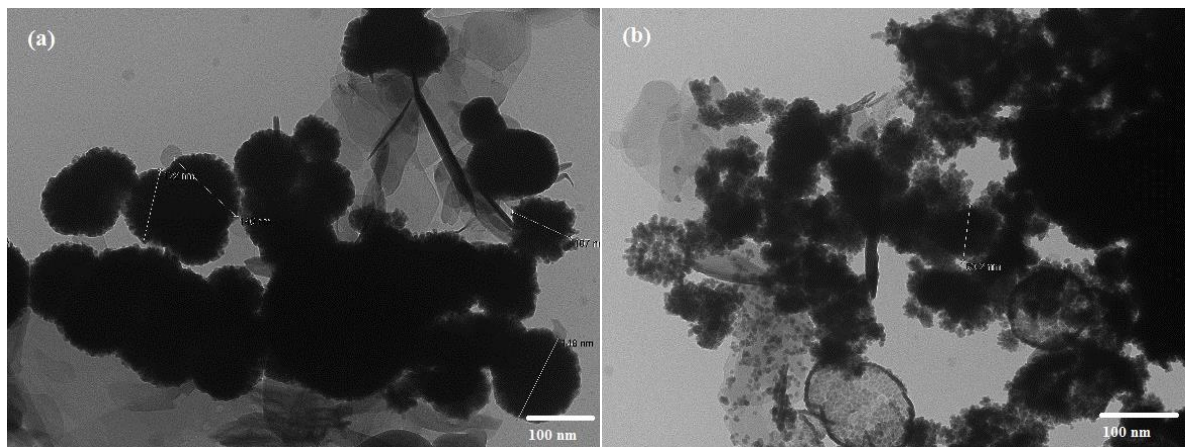
Figure 24. FeNi$_3$ (a) and FeNi$_3$-PVP nanoparticles produced via sequential reduction method.

From the morphological and elemental analysis of iron-nickel ANP synthesis via sequential reduction, it cannot be concluded that a core-shell morphology was achieved. Although certain structures appeared to have smaller particles formed around larger particles, the other varying structures are abundant. Final, resolved conclusions on the particle morphology from this reaction process cannot be made. Future studies should investigate a shortened reaction time to minimize the ability of varying particle structures, and test the effect of capping agents on the morphology of final nanostructures.

CHAPTER 5

CONCLUSION

A novel nanoparticle synthesis method was developed and applied to several transition metal and bimetallic systems, which have direct application for electronic devices, catalysis, and biomedicine. Monodispersed Ni nanoparticles were synthesized after a series of experiments by optimizing the reaction parameters including injection method, atmosphere, seeding, and reaction time. The parameters of this optimized method, called the standard method, include an argon-saturated aqueous solution, 1:2 molar ratio of M^{2+}: $NaBH_4$, 0.11 mL/min $NaBH_4$ injection rate over 45 min, 1 h of reaction time, and water/ethanol purification. This method was applied successfully to Fe and $FeNi_3$ alloy systems. Spherical Fe nanoparticles were synthesized, and it was observed that particles became smaller and denser during the 1-hour reaction period. $FeNi_3$ ANPs were produced using this method. Excessive metal oxide formation could not be overcome, limiting the applicability of these particles for electronic and catalytic applications. In these three systems, the particles self-assembled into chain-like aggregates. These different systems show the versatility of the standard method. Future work should evaluate its versatility with other transition metals.

The standard method was applied to make ZnO nanostructures, which have a potential application in electronic devices as an interfacial layer. In this system, zinc oxide was produced instead of elemental zinc. Similar to other metal nanoparticles synthesis described above, reaction parameters such as reagent molar ratio and reaction time were evaluated, but reproducible nanostructures were not observed. A final attempt was performed at an increased pH and with a 1:1 molar ratio of reagents. From this method, 6-

9 nm spherical nanoparticles self-assembled into single-particle thick hexagonal microplates. IR spectroscopy demonstrated significant amounts of $Zn(OH)_2$ were produced. SAED analysis indicated that particles were polycrystalline.

Other synthesis methods were investigated for in the preparation of $FeNi_3$ alloy system. A process derived from literature[31] was adjusted to fit our green synthesis standards with the goal of forming alloy nanoparticles with $FeNi_3$ core-shell morphology. The goal was not achieved through this or other synthesis methods attempted, but minimally aggregated, spherical, mixed ANPs with excellent reproducibility were produced. These particles were formed in an argon-saturated, basic, aqueous solution after a 12 h reaction period and ethanol purification. These alloy particles had very high oxygen atomic percentages that could not be reduced by any method attempted. Core-shell morphology was attempted by a sequential reduction method, but product morphology was inconsistent and results were inconclusive. Future work should be performed to prevent oxide formation so these particles could be viable for electronic and catalytic applications

Each alloy synthesis trial was performed twice—with and without PVP—to the study the effects of this capping agent on particle morphology. The standard method trial was the only sample in which a PVP shell was observed encapsulating the alloy particles. In other trials, no capping agent shell was observed, but nanoparticle diameter decreased in every experiment including PVP. In one trial, the concentration of capping agent was varied, and it was shown that particle diameter decreased with increasing PVP concentration. While this behavior is expected, it would be advantageous to investigate a more ideal environment for PVP capping. Consistent with other alloy experiments, metal

oxide formation was a significant problem in these trials, limiting the catalytic and electronic applications of MNPs.

Our future studies along these lines will focus on optimizing particle morphologies and dimensions using microwave synthesis and characterizing electrical properties of these metal particles and alloy nanocomposites.

REFERENCES

(1)   Duan, H.; Wang, D.; Li, Y. *Chem. Soc. Rev.* **2015**, *44* (16), 5778.

(2)   Ferrando, R.; Jellinek, J.; Johnston, R. L. *Chem. Rev.* **2008**, *108* (3), 845.

(3)   Kamat, P. V. *J. Phys. Chem. C* **2007**, *111* (7), 2834.

(4)   Mukherji, D. *Def. Sci. J.* **2016**, *66* (4), 291.

(5)   Moghimi, N.; Bazargan, S.; Pradhan, D.; Leung, K. T. *J. Phys. Chem. C* **2013**, *117* (9), 4852.

(6)   Schwartzberg, A. M.; Zhang, J. Z. *J. Phys. Chem. C* **2008**, *112* (28), 10323.

(7)   Deng, D.; Jin, Y.; Cheng, Y.; Qi, T.; Xiao, F. *ACS Appl. Mater. Interfaces* **2013**, *5* (9), 3839.

(8)   Vasilyeva, S. V.; Vorotyntsev, M. A.; Bezverkhyy, I.; Lesniewska, E.; Heintz, O.; Chassagnon, R. *J. Phys. Chem. C* **2008**, *112* (50), 19878.

(9)   Jadhav, A. H.; Patil, S. H.; Sathaye, S. D.; Patil, K. R. *J. Mater. Sci.* **2014**, *49* (17), 5945.

(10)   Sarkar, J.; Ghosh, M.; Mukherjee, A.; Chattopadhyay, D.; Acharya, K. *Bioprocess Biosyst. Eng.* **2014**, *37* (2), 165.

(11)   Li, W.; Sun, Y.; Xu, J. *Nano-Micro Lett.* **2012**, *4* (2), 98.

(12)   Rusen, E.; Mocanu, A.; Somoghi, R. *Colloid Polym. Sci.* **2012**, *290* (18), 1937.

(13)   Sepulveda-Guzman, S.; Reeja-Jayan, B.; de la Rosa, E.; Torres-Castro, A.; Gonzalez-Gonzalez, V.; Jose-Yacaman, M. *Mater. Chem. Phys.* **2009**, *115* (1), 172.

(14)   Yue, S.; Lu, J.; Zhang, J. *Mater. Chem. Phys.* **2009**, *117* (1), 4.

(15)   Senthilkumar, K.; Senthilkumar, O.; Morito, S.; Ohba, T.; Fujita, Y. *J. Nanoparticle Res.* **2012**, *14* (10).

(16)   Gunnarsson, R.; Helmersson, U.; Pilch, I. *J. Nanoparticle Res.* **2015**, *17* (9), 353.

(17)   Zhou, S.; Li, J.; Gilroy, K. D.; Tao, J.; Zhu, C.; Yang, X.; Sun, X.; Xia, Y. *ACS Nano* **2016**, *10* (11), 9861.

(18)   Nik Roselina, N. R.; Azizan, A.; Lockman, Z. *Sains Malays.* **2012**, *41* (8), 1037.

(19)   Guo, Y.; Azmat, M. U.; Liu, X.; Ren, J.; Wang, Y.; Lu, G. *J. Mater. Sci.* **2011**, *46* (13), 4606.

(20)   Grzelczak, M.; Pérez-Juste, J.; Mulvaney, P.; Liz-Marzán, L. M. *Chem. Soc. Rev.* **2008**, *37* (9), 1783.

(21)   Godfrey, I. J.; Dent, A. J.; Parkin, I. P.; Maenosono, S.; Sankar, G. *J. Phys. Chem. C* **2017**, *121* (3), 1957.

(22)   Wu, W.; Njoki, P. N.; Han, H.; Zhao, H.; Schiff, E. A.; Lutz, P. S.; Solomon, L.; Matthews, S.; Maye, M. M. *J. Phys. Chem. C* **2011**, *115* (20), 9933.

(23)   Peng, Z.; Spliethoff, B.; Tesche, B.; Walther, T.; Kleinermanns, K. *J. Phys. Chem. B* **2006**, *110* (6), 2549.

(24)   Liu, S.; Chen, G.; Prasad, P. N.; Swihart, M. T. *Chem. Mater.* **2011**, *23* (18), 4098.

(25)   Yang, X.; Roling, L. T.; Vara, M.; Elnabawy, A. O.; Zhao, M.; Hood, Z. D.; Bao, S.; Mavrikakis, M.; Xia, Y. *Nano Lett.* **2016**, *16* (10), 6644.

(26)   Lay, M. D.; Stickney, J. L. *J. Am. Chem. Soc.* **2003**, *125* (5), 1352.

(27)   Reiss, B. D.; Mao, C.; Solis, D. J.; Ryan, K. S.; Thomson, T.; Belcher, A. M. *Nano Lett.* **2004**, *4* (6), 1127.

(28)   Liang, Y.; Liu, P.; Yang, G. *Cryst. Growth Des.* **2014**, *14* (11), 5847.

(29)   Teeriniemi, J.; Melander, M.; Lipasti, S.; Hatz, R.; Laasonen, K. *J. Phys. Chem. C*
        2017, *121* (3), 1667.

(30)   Jia, J.; Yu, J. C.; Wang, Y.-X. J.; Chan, K. M. *ACS Appl. Mater. Interfaces* **2010**, *2*
        (9), 2579.

(31)   Zhou, J.; Jiao, T.; Guo, W.; Wang, B.; Guo, H.; Cui, L.; Zhang, Q.; Chen, Y.;
        Peng, Q. *Nanomater. Nanotechnol.* **2015**, *5*, 25.

(32)   Hongxia, G.; Hua, C.; Fan, L.; Zhenping, Q.; Suping, C.; Zuoren, N. *J. Mater. Res.*
        2012, *27* (11), 1522.

(33)   Zhou, X.-M.; Wei, X.-W. *Cryst. Growth Des.* **2009**, *9* (1), 7.

(34)   Suh, Y. J.; Jang, H. D.; Chang, H.; Kim, W. B.; Kim, H. C. *Powder Technol.* **2006**,
        161 (3), 196.

(35)   Lu, X.; Liang, G.; Zhang, Y. *Mater. Sci. Eng. B* **2007**, *139* (2–3), 124.

(36)   Wang, H.; Li, J.; Kou, X.; Zhang, L. *J. Cryst. Growth* **2008**, *310* (12), 3072.

(37)   Liu, L.; Guan, J.; Shi, W.; Sun, Z.; Zhao, J. *J. Phys. Chem. C* **2010**, *114* (32),
        13565.

(38)   Wang, J.; Jia, X.; Zhou, J.; Pan, L.; Huang, S.; Chen, X. *ACS Appl. Mater.*
        Interfaces **2016**, *8* (39), 26098.

(39)   Mohan, P.; Takahashi, M.; Higashimine, K.; Mott, D.; Maenosono, S. *Langmuir*
        2017.

(40)   Nugroho, F. A. A.; Iandolo, B.; Wagner, J. B.; Langhammer, C. *ACS Nano* **2016**,
        10 (2), 2871.

(41)   Huang, D.; Liao, F.; Molesa, S.; Redinger, D.; Subramanian, V. *J. Electrochem.*
        Soc. **2003**, *150* (7), G412.

(42) Morisada, Y.; Nagaoka, T.; Fukusumi, M.; Kashiwagi, Y.; Yamamoto, M.; Nakamoto, M. *J. Electron. Mater.* **2010**, *39* (8), 1283.

(43) Chen, Y.; Peng, D.-L.; Lin, D.; Luo, X. *Nanotechnology* **2007**, *18* (50), 505703.

(44) Liu, Z.; Li, S.; Yang, Y.; Peng, S.; Hu, Z.; Qian, Y. *Adv. Mater.* **2003**, *15* (22), 1946.

(45) Ely, T. O.; Amiens, C.; Chaudret, B.; Snoeck, E.; Verelst, M.; Respaud, M.; Broto, J.-M. *Chem. Mater.* **1999**, *11* (3), 526.

(46) Li, D.; Komarneni, S. *J. Am. Ceram. Soc.* **2006**, *89* (5), 1510.

(47) Swihart, M. T. *Curr. Opin. Colloid Interface Sci.* **2003**, *8* (1), 127.

(48) Tsuzuki, T.; McCormick, P. G. *J. Mater. Sci.* **2004**, *39* (16), 5143.

(49) Iravani, S. *Green Chem.* **2011**, *13* (10), 2638.

(50) Huang, K.-C.; Ehrman, S. H. *Langmuir* **2007**, *23* (3), 1419.

(51) Park, J.; Lee, E.; Hwang, N.-M.; Kang, M.; Kim, S. C.; Hwang, Y.; Park, J.-G.; Noh, H.-J.; Kim, J.-Y.; Park, J.-H.; Hyeon, T. *Angew. Chem. Int. Ed.* **2005**, *44* (19), 2872.

(52) Huber, D. *Small* **2005**, *1* (5), 482.

(53) Zhang, G.; Liao, Y.; Baker, I. *Mater. Sci. Eng. C* **2010**, *30* (1), 92.

(54) Chung, Y. T.; Ba-Abbad, M. M.; Mohammad, A. W.; Hairom, N. H. H.; Benamor, A. *Mater. Des.* **2015**, *87*, 780.

(55) Omri, K.; Najeh, I.; Dhahri, R.; El Ghoul, J.; El Mir, L. *Microelectron. Eng.* **2014**, *128*, 53.

(56) Pan, Z. W.; Dai, Z. R.; Wang, Z. L. *Science* **2001**, *291*, 1947.

(57) dos Santos, C. M.; Martins, A. F. N.; Costa, B. C.; Ribeiro, T. S.; Braga, T. P.; Soares, J. M.; Sasaki, J. M. *J. Nanomater.* **2016**, *2016*, 1.

(58) Niu, Z.; Li, Y. *Chem. Mater.* **2014**, *26* (1), 72.

(59) Xu, S.; Wang, Z. L. *Nano Res.* **2011**, *4* (11), 1013.

(60) Bharde, A.; Rautaray, D.; Bansal, V.; Ahmad, A.; Sarkar, I.; Yusuf, S. M.; Sanyal, M.; Sastry, M. *Small* **2006**, *2* (1), 135.

(61) Ali, A.; Zafar, H.; Zia, M.; ul Haq, I.; Phull, A. R.; Ali, J. S.; Hussain, A. *Nanotechnol. Sci. Appl.* **2016**, *9*, 49.

(62) WANG, R.-H.; JIANG, J.-S.; HU, M. *Acta Phys.-Chim. Sin.* **2009**, *25* (10), 2167.

(63) Yu, J.; Yu, X. *Environ. Sci. Technol.* **2008**, *42* (13), 4902.

(64) Jang, J.-M.; Kim, S.-D.; Choi, H.-M.; Kim, J.-Y.; Jung, W.-G. *Mater. Chem. Phys.* **2009**, *113* (1), 389.

(65) Brinker, C. J.; Scherer, G. W. *Sol-gel science: the physics and chemistry of sol-gel processing*; Academic Press: Boston, 1990, 2-10

(66) Chen, D.-H.; Wu, S.-H. *Chem. Mater.* **2000**, *12* (5), 1354.

(67) Balakrishnan, S.; Bonder, M. J.; Hadjipanayis, G. C. *J. Phys. Appl. Phys.* **2009**, *42* (24), 245005.

(68) Chou, L.-H.; Hung, W.-C.; Lee, M.-T. *Mater. Sci.* **2016**, *22* (2).

(69) Ilari, G. M.; Kränzlin, N.; Longtin, R.; Sanchez-Valencia, J. R.; Schneider, S.; Rossell, M. D.; Niederberger, M.; Erni, R. *Carbon* **2014**, *73*, 146.

(70) Eluri, R.; Paul, B. *J. Nanoparticle Res.* **2012**, *14* (4).

(71) Polte, J. *CrystEngComm* **2015**, *17* (36), 6809.

(72) Zhang, Z.; Wang, Z.; He, S.; Wang, C.; Jin, M.; Yin, Y. *Chem. Sci.* **2015**, *6* (9), 5197.

(73) Miura, A.; Wang, H.; Leonard, B. M.; Abruña, H. D.; DiSalvo, F. J. *Chem. Mater.* **2009**, *21* (13), 2661.

(74) Green, M. A.; Emery, K.; Hishikawa, Y.; Warta, W.; Dunlop, E. D. *Prog. Photovolt. Res. Appl.* **2014**, *22* (1), 1.

(75) Wright, M.; Uddin, A. *Sol. Energy Mater. Sol. Cells* **2012**, *107*, 87.

(76) Hwan Jung, H.; Ho Kim, D.; Su Kim, C.; Bae, T.-S.; Bum Chung, K.; Yoon Ryu, S. *Appl. Phys. Lett.* **2013**, *102* (18), 183902.

(77) Panwbrinar, N. L.; Kaushik, S. C.; Kothari, S. *Renew. Sustain. Energy Rev.* **2011**, *15* (3), 1513.

(78) Zhang, Q.; Sun, Y.; Xu, W.; Zhu, D. *Adv. Mater.* **2014**, *26* (40), 6829.

(79) Carrete, J.; Mingo, N.; Tian, G.; Ågren, H.; Baev, A.; Prasad, P. N. *J. Phys. Chem. C* **2012**, *116* (20), 10881.

(80) Rao, K. S.; Balaji, T.; Lingappa, Y.; Reddy, M. R. P.; Prakash, T. L. *Phase Transit.* **2012**, *85* (3), 235.

(81) Wang, H. T.; Ye, Y. Y.; Qi, J.; Li, F. T.; Tang, Y. L. *Water Sci. Technol.* **2013**, *68* (5), 1137.

(82) Abeywickrama, T.; Sreeramulu, N. N.; Xu, L.; Rathnayake, H. *RSC Adv.* **2016**, *6* (94), 91949.

(83) Sowri Babu, K.; Ramachandra Reddy, A.; Sujatha, C.; Venugopal Reddy, K.; Mallika, A. N. *J. Adv. Ceram.* **2013**, *2* (3), 260.